Durham E-Theses

Zeeman-tunable Modulation Transfer Spectroscopy

SO, CHLOE

How to cite:

SO, CHLOE (2020) *Zeeman-tunable Modulation Transfer Spectroscopy*, Durham theses, Durham University. Available at Durham E-Theses Online: http://etheses.dur.ac.uk/13481/

Zeeman-tunable Modulation Transfer Spectroscopy

Chloe So

A thesis submitted in partial fulfilment
of the requirements for the degree of
Master of Science by Research

Department of Physics
Durham University

4th March 2020

Dedicated to

He who died for me on the cross

Zeeman-tunable Modulation Transfer Spectroscopy

Chloe So

Active frequency stabilization of a laser to an atomic or molecular resonance underpins many modern-day AMO physics experiments. With a flat background and high signal-to-noise ratio, modulation transfer spectroscopy (MTS) offers an accurate and stable method for laser locking. Despite its benefits, however, the four-wave mixing process that is inherent to the MTS technique entails that the strongest modulation transfer signals are only observed for closed transitions, excluding MTS from numerous applications. Here, we report for the first time the observation of a magnetically tunable MTS error signal. Using a simple two-magnet arrangement, we show that the error signal for the ^{87}Rb $F = 2 \to F' = 3$ cooling transition can be Zeeman-shifted over a range of $\sim 10\,\mathrm{GHz}$ to any arbitrary point on the rubidium D_2 spectrum. Modulation transfer signals for locking to the ^{87}Rb $F = 1 \to F' = 2$ repumping transition as well as $1\,\mathrm{GHz}$ red-detuned to the cooling transition are presented to demonstrate the versatility of this technique, which can readily be extended to the locking of Raman and lattice lasers.

Declaration

I confirm that no part of the material offered has previously been submitted by myself for a degree in this or any other University. Where material has been generated through joint work, the work of others has been indicated.

Chloe So
in Durham, on 4th March 2020

Acknowledgements

First and foremost I would like to thank my supervisor, Professor Charles Adams, for taking me in despite my lack of experience in experimental physics. I am grateful to him for the past twelve months, which in many ways have been the highlight of my four years in Durham. Without his creativity, patience and knowledge, this thesis could not have been born at all.

Then, in order of appearance (except for Teodora who, despite I met during my first visit, had been absent for the better half of my time here): I thank Nick for showing me the rails when I knew nearly nothing. His support and guidance have been instrumental in the evolution of the project, and have helped me become a better researcher.

A big thank you goes to Charles also for teaching me physics, for answering my many questions even when it meant he will miss grocery shopping, and most importantly for being a good friend. His almost intuitive understanding of and enthusiasm towards physics continues to inspire me greatly.

My thanks are also due to Chris, whose wealth of experimental knowledge and companionship I relied on almost daily. His eagerness to take up something new as well as dedication to his work are evident in every aspect of the experiment. I will miss being his secretary (unofficially) very much.

This wouldn't be a proper acknowledgement without thanking Teodora, by the way. Being the oldest member in the lab, she emanates motherly love and warmth (and occasionally smoke) wherever she goes, and makes going to work every day a lot of fun.

Thank you also to the lunch gang—Niamh, Parvez, Shuying and Sofia. Our many and varied conversation topics (which can range from the difference between bees and wasps to Bulgarian yoghurt) never cease to amaze me. I also thank the wider QLM group for being a thriving yet welcoming environment, it has been a pleasure working with everyone.

Contents

List of Figures

1 Introduction

1.1 Motivation

It is no exaggeration to say that, ever since its advent in the early 1960s, the laser has exerted tremendous influence on the direction of modern physics research. This is especially true in the field of atomic, molecular and optical (AMO) physics, where the laser—due to its ability to produce intense, coherent, tunable and monochromatic light—has replaced lamps to become the primary source of optical radiation.

Expedited by this laser revolution, much of present-day AMO physics research revolves around the interaction of light and matter in one fashion or another. Laser sources that can be tuned to particular atomic transitions are now a workhorse tool in nearly every atomic physics laboratory, with their most prominent uses being in optical pumping, high precision spectroscopy, laser cooling and trapping, etc. For many such applications, active frequency stabilisation (or, more conventionally, 'locking') of the laser to some stable reference, is paramount. Many a time, it is necessary that the laser be stabilised to well below the natural linewidth of a transition, e.g. to less than a few hundred kilohertz in the care of alkali metal D-transitions.

To this end, a myriad of spectroscopic techniques have been developed. These include single-beam methods such as dichroic atomic vapour laser locking (DAVLL) [1–3]; and pump-probe schemes such as saturation absorption spectroscopy (SAS) [4], polarisation spectroscopy (PS) [5, 6], frequency modulation spectroscopy (FMS) [7], and modulation transfer spectroscopy (MTS) [8–10]. While their names might sound a mouthful, the common idea behind these approaches is simple: to generate a dispersive error signal whose zero-crossing is centered on an atomic resonance, and which can be used to provide a feedback for locking the laser.

Of those outlined above, FMS and MTS have emerged as two of the most popular laser locking techniques. However, MTS is often preferable to FMS for two important reasons [Fig. 1.1]: firstly, the method readily creates dispersive-like lineshapes that reside on a symmetric, Doppler-free background. Secondly, the generated signal is suppressed for open transitions and undesirable crossover features arising from the pump-probe scheme. The resultant spectrum is 'clean', displaying strong signals with unambiguous zero-crossings at closed transitions only.

The second feature is particularly useful in the event that the frequency spacing between consecutive transitions is small, as is usually the case in the alkali metals,
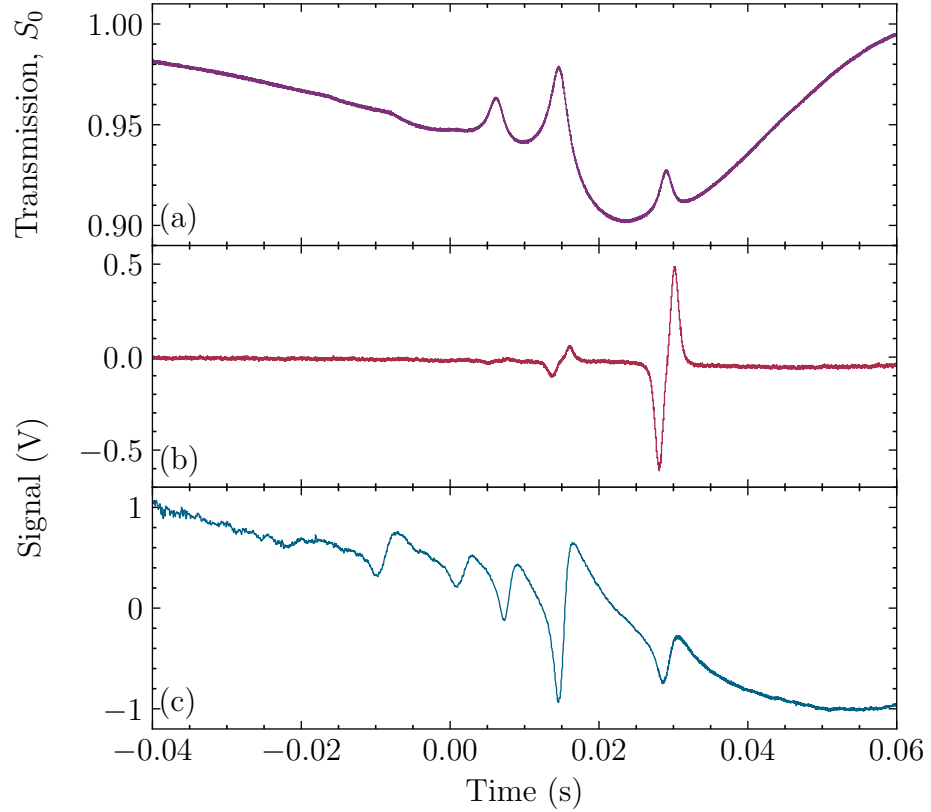
Figure 1.1 | Comparison between (b) modulation transfer spectroscopy and (c) frequency modulation transfer spectroscopy for the ^{87}Rb $F = 2 \rightarrow F' = 3$ cooling transition. The saturation absorption spectrum is shown in (a) for completion.

but also presents a problem when one wishes to lock *away* from the closed transition—an example being the ^{87}Rb $F = 1 \rightarrow F' = 2$ repumping transition. FMS is advantageous in this regard, as it is able to produce error signals for all sub-Doppler features with amplitudes corresponding to those in the saturation absorption spectrum. Notwithstanding this, the non-zero background that accompanies the FMS technique means that the lock point is at risk of 'hopping' (amongst other pathologies) from one transition to another.

In answer to the above, and following growing interest in performing thermal vapour experiments in the hyperfine Paschen–Back regime [11–20], here we present a technique to shift the MTS error signal in the presence of a large magnetic field. This method exploits the Zeeman effect, wherein the spectral line of an atom can be split in the presence of an external magnetic field; as well as the fact that so long as a transition is closed we obtain a modulation transfer lineshape, to produce multiple 'copies' of lock signals that are magnetically tunable. Specifically, we will show that it is possible to Zeeman-shift the MTS signal for the ^{87}Rb $F = 2 \rightarrow F' = 3$ 'cooling' transition by ± 8 GHz, including onto the ^{87}Rb $F = 1 \rightarrow F' = 2$ 'repumping' transition, using a 4.7 kG magnetic field.

It is worth mentioning before going any further that, though the application of bias fields to spectroscopy setups is not new, previous demonstrations lack either the high signal-to-noise ratio of the MTS technique [21, 22], or the flexibility of

having a widely-tunable stabilised source that is the focus of this work [23, 24]. This contrasts with the proposed method which, aside from preserving all the aforenarrated advantages of MTS, has the additional benefits of being highly adaptable and reproducible.

Another point to note is that, while tuning can also be achieved with acousto-optical modulators (AOMs), this tuning is often fixed and in the few hundred MHz range. There is also the fact that much efficiency is lost over these components, and that they tend to be prohibitively expensive. In the same vein, though a range of very flexible beat-locking methods exist to accomplish widely tunable offset locking, not infrequently it is sufficient that the lock frequency maintains some stable offset from the atomic reference. On such occasions, the introduction of an additional reference laser in the master–slave configuration adds to the system not only complexity but cost, especially when only one laser frequency is needed. This extra layer of complication and expense is not required with Zeeman-tunable modulation transfer spectroscopy.

1.2   Thesis structure

The thesis is structured as follows:

- **Chapter 2**, in which the basic theory modulation transfer spectroscopy and the Zeeman effect are laid out. The chapter ends with a proposal of how the combination of the two can be used to improve the existing MTS scheme.

- **Chapter 3**, in which the experimental apparatus and techniques used to carry out the investigations in this thesis are detailed. Specifically, we will show the designs for the 2 mm Rb vapour cell, the heat-resistant holder in which it is to be placed, as well as the permanent magnets which provide the external field.

- **Chapter 4**, in which we demonstrate Zeeman-tunable modulation transfer spectroscopy, i.e. that the error signal for the ^{87}Rb $F = 2 \rightarrow F' = 3$ cooling transition can be arbitrarily translated on the rubidium D_2 spectrum by virtue of a large axial magnetic field. We also show the theoretically predicted Zeeman-shift and linewidth as compared to the experimentally measured values.

- **Chapter 5**, in which we draw our conclusions. Potential applications and areas for improvement will also be discussed.

1.3   Publications

Publications arising from this work

- C. So, N. L. R. Spong, C. Möhl, Y. Jiao, T. Ilieva, and C. S. Adams, Zeeman-tunable modulation transfer spectroscopy, Opt. Lett. **44**, 5374–5377 (2019)

Related publications

- C. Möhl, N. L. R. Spong, Y. Jiao, C. So, T. Ilieva, M. Weidemüller, and C. S. Adams, Photon correlation transients in a weakly blockaded Rydberg ensemble, arXiv:1910.13155 [physics] (2019). To appear in J. Phys. B: At. Mol. Opt. Phys. (2020)

2 Theory

2.1 Modulation transfer spectroscopy

Based upon standard saturation absorption spectroscopy, modulation transfer spectroscopy is a pump-probe method that generates sub-Doppler lineshapes well suited for laser locking. The experimental layout for MTS is shown in Fig. 3.1(b). By convention, we shall denote the two counter-propagating laser beams as the pump and probe.

In MTS, the phase of the pump beam is modulated by an electro-optic modulator (EOM) or an acousto-optic modulator (AOM). The transmitted light can be expressed by

$$
\begin{aligned}
E_{\text{pump}} &= E_0 \sin(\omega_{\text{c}} t + \delta \sin \omega_{\text{m}} t) \\
&= E_0 \left[\sum_{n=0}^{\infty} J_n(\delta) \sin(\omega_{\text{c}} + n\omega_{\text{m}})t + \sum_{n=1}^{\infty} (-1)^n J_n(\delta) \sin(\omega_{\text{c}} - n\omega_{\text{m}})t \right],
\end{aligned}
\tag{2.1.1}
$$

where ω_{c} is the carrier wave frequency, ω_{m} is the modulation frequency, δ is the modulation index, and $J_n(\delta)$ is the n-th order Bessel function.

If the interactions of the pump and probe with the atomic vapour are sufficiently non-linear, sidebands will appear on the counter-propagating probe field $E_{\text{probe}} = E_0 \sin(\omega_{\text{c}} t)$. This transfer of modulation has been described as an example of degenerate four-wave mixing (FWM) [27, 28], whereby in a three-photon excitation process—successively, absorption, emission, and absorption—a fourth photon carrying the modulated amplitude and phase shift is emitted along the direction of the probe [Fig. 2.1]. Then the MTS signal, which is a function of the detuning from the atomic transition Δ, is given by the beating between the generated sidebands and the probing light [29]:

$$
\begin{aligned}
S_{\delta,\omega_{\text{m}},\phi}(\Delta) = &\frac{C}{\sqrt{\Gamma^2 + \omega_{\text{m}}^2}} \sum_{n=-\infty}^{\infty} J_n(\delta) J_{n-1}(\delta) \\
&\times [(L_{(n+1)/2} + L_{(n-2)/2}) \cos(\omega_{\text{m}} t + \phi) \\
&+ (D_{(n+1)/2} - D_{(n-2)/2}) \sin(\omega_{\text{m}} t + \phi)].
\end{aligned}
\tag{2.1.2}
$$

In this expression, Γ is the natural linewidth of the excited state, ϕ is the detector phase relative to the modulation applied to the pump, C is a constant dependent

on the photodiode detection parameters and laser intensity, and

$$L_n(\Delta) = \frac{\Gamma^2}{\Gamma^2 + (\Delta - n\omega_{\mathrm{m}})^2}, \quad D_n(\Delta) = \frac{\Gamma(\Delta - n\omega_{\mathrm{m}})}{\Gamma^2 + (\Delta - n\omega_{\mathrm{m}})^2}, \tag{2.1.3}$$

specify the absorption and dispersion of the medium, respectively. Typically $\delta < 1$, so considering only the first-order sidebands Eqn. 2.1.2 can be simplified to

$$\begin{aligned} S_{\delta,\omega_{\mathrm{m}},\phi}(\Delta) = &\frac{C}{\sqrt{\Gamma^2 + \omega_{\mathrm{m}}{}^2}} J_0(\delta) J_1(\delta) \\ &\times [(L_{-1} - L_{-1/2} + L_{1/2} - L_1)\cos(\omega_{\mathrm{m}}t + \phi) \\ &+ (D_1 - L_{1/2} - L_{-1/2} + L_{-1})\sin(\omega_{\mathrm{m}}t + \phi)]. \end{aligned} \tag{2.1.4}$$

Two observations can be made from the above: firstly, by varying the phase shift ϕ between the sine and cosine terms (from 0 to $\pi/2$), the absorption and dispersion components of the spectroscopic signal, as well as a combination of the two forms, can be retrieved using a phase-sensitive detector. Secondly, pairwise comparison of the terms in n and $-1 + n$ yields that $S_{\delta,\omega_{\mathrm{m}},\phi}(\Delta)$ is always an odd function in Δ, and that $S(0) = 0$. Practically this has the meaning that, in the resultant signal, negative detunings are seen as increases in amplitude, positive detunings are seen as decreases in amplitude, while the line centre is represented as a zero-crossing.

(a)

(b)
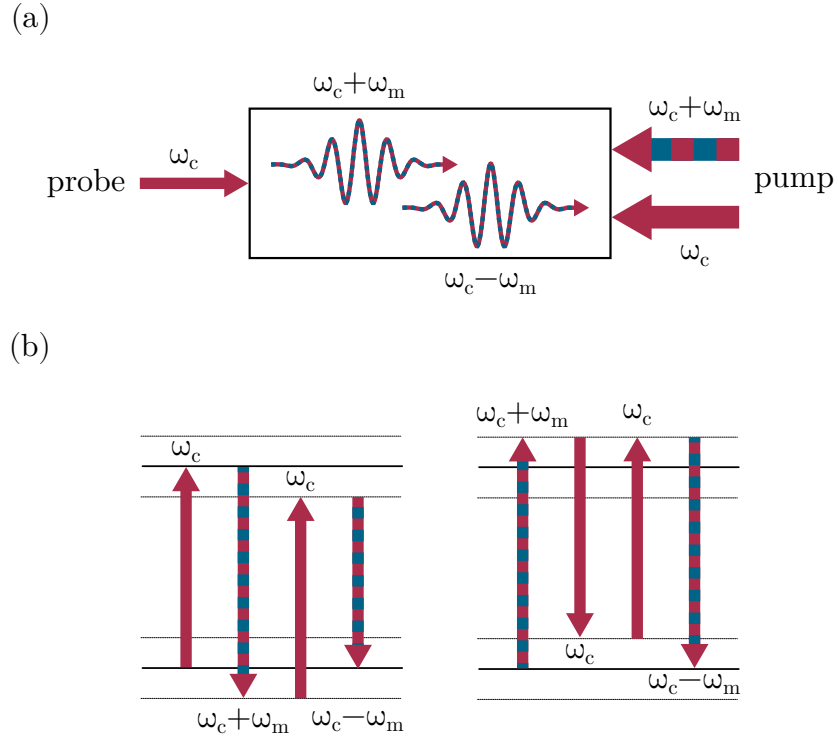
Figure 2.1 | Pictorial illustration of four-wave mixing in MTS (a), in which two frequency components of the pump beam combine with the counter-propagating probe to generate a fourth wave in the direction of the latter (b). Modulation on the carrier frequency is shown in the figure as blue stripes. In this example we considered only the $\omega_{\mathrm{c}} + \omega_{\mathrm{m}}$ sideband, but the same applies to its $\omega_{\mathrm{c}} - \omega_{\mathrm{m}}$ counterpart.

It is interesting to point out that, much of the competitive edge MTS possesses comes from the FWM process. To begin with, the MTS method readily creates dispersive-like signals that reside on a symmetric, Doppler-free background. The reason is that, whereas FMS relies on the direct detection of vapour absorption and dispersion by the modulated probe beam, the MTS signal originates from the frequency-dependent FWM process in which the probability of the stimulated four-photon transition falls off rapidly away from resonance. The lineshape baseline stability thus becomes insensitive to the residual linear-absorption of the medium, and is immune to dispersive elements (e.g. parasitic etalons) which can alter the location of the lock-point by adding an offset to the demodulated error signal. The zero-crossings of the modulation transfer signals are accurately centered on the corresponding hyperfine peaks, providing stable, unambiguous frequency references to which the laser can be locked.

Another reason to prefer MTS-based laser locking is that the generated signal is suppressed for open transitions and undesirable crossover features arising from the pump-probe scheme. This is as a result of the FWM process only being efficient for closed transitions, where dissipation to atomic states other than the ground state is minimal and the interaction time between atom and light is long [30, 31]. The resultant spectrum is 'clean', displaying strong signals with steep gradients for closed transition lines only. Whilst this can be useful in the event that the frequency spacing between consecutive transitions is small, as is usually the case in the alkali metals, it also presents a problem when one wishes to lock *away* from the closed transition—an example of this is the ^{87}Rb $F = 1 \rightarrow F' = 2$ repumping transition. FMS is advantageous in this regard, as it is able to produce error signals for all sub-Doppler features with amplitudes corresponding to those in the saturation absorption spectrum. Be that as it may, the non-zero background that accompanies the FMS technique means that the lock point is at risk of 'hopping' (amongst other pathologies) from one transition to another.

2.2 Atom-light interactions in magnetic fields

2.2.1 ^{87}Rb atomic structure

We now turn to consider the electronic structure of rubidium 87, which is crucial to the understanding of the underlying physics of the experiment. Akin to atomic hydrogen, rubidium is a Group I element with a single electron in the valence orbital. Naturally occuring rubidium have two isotopes: ^{85}Rb (72.2%) with nuclear spin $I = 5/2$, and ^{87}Rb (28.8%) with $I = 3/2$. A detailed analysis of the structure of the alkali metals can be found in most atomic physics text books (e.g., Ref. [32]), but for the sake of completeness we cite here a few of the key findings.

2.2.1.1 Fine structure

The level structure diagram of the ^{87}Rb D$_2$ transition which, jointly with the D$_1$ transition form a fine-structure doublet, is shown in Fig. 2.2. The fine structure
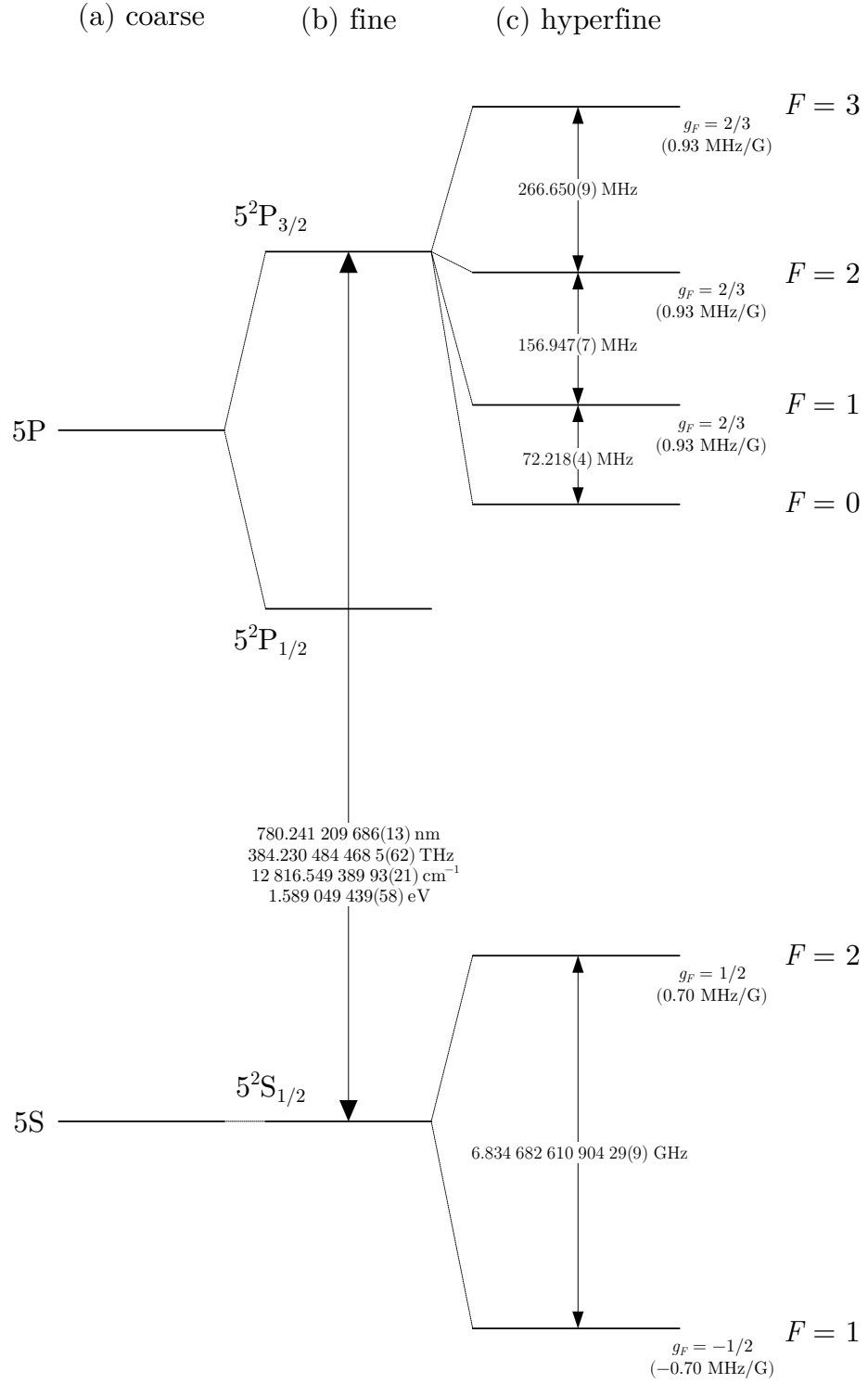
(a) coarse   (b) fine   (c) hyperfine

Figure 2.2 | Unperturbed (a) coarse, (b) fine, and (c) hyperfine structure diagram of the ^{87}Rb D$_2$ transition. The approximate Landé g_F-factors for each individual F state are given, along with the Zeeman splittings between adjacent m_F levels. Adapted from [33].

splitting is a result of the coupling between the orbital angular momentum of the outermost electron $\mathbf{L}$ and its spin angular momentum $\mathbf{S}$:

$$\mathbf{J} = \mathbf{L} + \mathbf{S} \tag{2.2.5}$$

where $\mathbf{J}$ is the total electron angular momentum and the permitted values of $J = |\mathbf{J}|$ are

$$|L - S| \leq J \leq L + S. \tag{2.2.6}$$

For the ^{87}Rb ground state, $L = 0$ and $S = 1/2$, so $J = |0 - 1/2|, ..., (0 + 1/2) = 1/2$. There is only one possible value of J, and because the energy of any particular level is shifted with respect to this value, the ground state has no fine structure. This is not the case for the first excited state, which has $L = 1$ and consequently $J = 1/2$ or $3/2$. Using the $n^{2S+1}L_J$ notation, the term symbol for the single ground state is $5^2\mathrm{S}_{1/2}$, whereas the two possibilities for the excited state are labelled $5^2\mathrm{P}_{1/2}$ and $5^2\mathrm{P}_{3/2}$ [Fig. 2.2(b)].

We define the two possible transitions from the ground to either of the $J = 1/2$ or $J = 3/2$ state as the ^{87}Rb 'D$_1$' and 'D$_2$' transitions, accordingly. In the absence of any external fields (electric and magnetic), the two lines are separated by approximately 7.1 THz, which is sufficiently large to be resolved by most lasers. In the context of this thesis, we shall look only at the D$_2$ transition.

2.2.1.2 Hyperfine structure

In addition to fine structure, there exists a much smaller effect in the D$_2$ transition named the 'hyperfine' structure—this is a consequence of the further coupling of $\mathbf{J}$ with the total nuclear angular momentum $\mathbf{I}$. The total atomic angular momentum $\mathbf{F}$ is then given by

$$\mathbf{F} = \mathbf{J} + \mathbf{I}. \tag{2.2.7}$$

As above, the magnitude of $\mathbf{F}$ falls in the range

$$|J - I| \leq F \leq J + I, \tag{2.2.8}$$

and its projection onto the quantisation axis, m_F, can take values

$$-F, (-F+1), ..., (F-1), F. \tag{2.2.9}$$

For the ground state in ^{87}Rb, $J = 1/2$ and $I = 3/2$, so $F = 1$ or 2. This splits the ground state into two levels separated by 6.83 GHz, which can be seen from the bottom half of Fig. 2.2(c). For the $F = 1$ level there are $2F + 1 = 3$ degenerate states $m_F = -1, 0, +1$; whereas $F = 2$ has 5 degenerate states $m_F = -2, -1, 0, +1, +2$.

For the excited state ($5^2\mathrm{P}_{3/2}$), the possible values of F range from $|3/2 - 3/2| = 0$ to $|3/2 + 3/2| = 3$. These levels (top half of Fig. 2.2(c)) are separated in frequency by 495.81 MHz, which is smaller than the Doppler width even at room temperature and is therefore unresolved. In zero magnetic field, the degeneracy of each of the

individual F state occurs as follows:

$$F = 0, \ m_F = 0$$
$$F = 1, \ m_F = -1, 0, +1$$
$$F = 2, \ m_F = -2, -1, 0, +1, +2$$
$$F = 3, \ m_F = -3, -2, -1, 0, +1, +2, +3.$$

In the section to come, we are going to see this degeneracy of the m_F states lifted in the presence of an external magnetic field.

2.2.2 The Zeeman effect

The energy levels of an atom shift in response to an applied magnetic field $\mathbf{B}$ in an effect known as Zeeman splitting. This is due to the coupling of the field to the electron orbital motion, the electron spin, and to the nuclear spin via [32]

$$\hat{\mathcal{H}}_B = -\frac{\mu_\mathrm{B}}{\hbar}(g_L \mathbf{L} + g_S \mathbf{S} + g_I \mathbf{I}) \cdot \mathbf{B}, \tag{2.2.10}$$

where μ_B is the Bohr magneton, and $g_{L,S,I}$ are the g-factors that account for various modifications to the corresponding magnetic dipole moments. $\hat{\mathcal{H}}_B$ is a term in the atomic Hamiltonian $\hat{\mathcal{H}}$:

$$\hat{\mathcal{H}} = \hat{\mathcal{H}}_0 + \hat{\mathcal{H}}_\mathrm{fs} + \hat{\mathcal{H}}_\mathrm{hfs} + \hat{\mathcal{H}}_\mathrm{B} \tag{2.2.11}$$

with $\hat{\mathcal{H}}_0$, $\hat{\mathcal{H}}_\mathrm{fs}$, and $\hat{\mathcal{H}}_\mathrm{hfs}$ defining respectively the coarse, fine, and hyperfine interactions; and together the unperturbed Hamiltonian of the atom.

In the absence of any external fields, the expectation value of each respective operator $\hat{\mathcal{H}}_0 \gg \hat{\mathcal{H}}_\mathrm{fs} \gg \hat{\mathcal{H}}_\mathrm{hfs}$, and the expectation value for the operator $\hat{\mathcal{H}}_\mathrm{B} = 0$.

2.2.2.1 Weak field

As the field strength increases, we cross into the weak field regime where the expectation values of $\hat{\mathcal{H}}_\mathrm{fs} \gg \hat{\mathcal{H}}_\mathrm{hfs} \gg \hat{\mathcal{H}}_\mathrm{B}$, and $\hat{\mathcal{H}}_\mathrm{B} \neq 0$ act as a perturbation to the zero-field eigenstates of $\hat{\mathcal{H}}_\mathrm{hfs}$. $\mathbf{J}$ and $\mathbf{I}$ couple to one another via $\mathbf{F} = \mathbf{J} + \mathbf{I}$, such that F and its projection m_F appropriately describe the bunching of the energy levels. The magnetic field component of the Hamiltonian, $\hat{\mathcal{H}}_\mathrm{B}$, is given by

$$\hat{\mathcal{H}}_B = -\frac{\mu_\mathrm{B}}{\hbar}(g_L \mathbf{L} + g_S \mathbf{S}) \cdot \mathbf{B}, \tag{2.2.12}$$

in which the nuclear term is neglected because $g_I \ll g_{L,S}$. In this regime, known as the *hyperfine linear Zeeman* (HLZ) regime [34], the energy levels shift proportionally to the magnetic field strength B according to

$$\Delta E_{|F \ m_F\rangle} = \mu_\mathrm{B} g_F m_F B. \tag{2.2.13}$$

This is the anomalous Zeeman effect.

2.2.2.2 Intermediate and strong fields

When the coupling to the external field becomes similar in strength to the hyperfine interaction, i.e. the expectation value of $\hat{\mathcal{H}}_{\text{hfs}} \sim \hat{\mathcal{H}}_{\text{B}}$, we are said to have entered the intermediate regime. The relationship between the shift and the magnetic field is no longer linear, and the lines begin to curve since neither of the two effects dominate. In this intermediate regime it is often said that there are no 'good' quantum numbers, which means that the relevant eigenstates cannot be described by a single of the L, S, J, I or F quantum number or its projection m.

If the magnetic field is sufficiently strong that the expectation value of $\hat{\mathcal{H}}_{\text{B}}$ greatly exceeds that of $\hat{\mathcal{H}}_{\text{hfs}}$, **J** and **I** decouple as individually they couple more strongly to the field than to each other. In this *hyperfine Paschen–Back* (HPB) regime, F and m_F are no longer valid quantum numbers, and the eigenfunctions of the atomic state are best represented with the total angular momentum J, m_J and nuclear spin I, m_I quantum numbers. The interaction Hamiltonian $\hat{\mathcal{H}}_{\text{B}}$ is given by

$$\hat{\mathcal{H}}_B = -\frac{\mu_{\text{B}}}{\hbar}(g_J \mathbf{J} + g_I \mathbf{I}) \cdot \mathbf{B}. \tag{2.2.14}$$

At still larger fields, there are the Paschen–Back and normal Zeeman regimes for the fine structure, where even J cannot be called a good quantum number. Nonetheless, this is nowhere in the vicinity of the states and field strengths considered in this thesis, and so are beyond the scope of the present discussion.

In numerically solving for the eigenvalues of the Hamiltonian for each value of B, the splitting of the energy levels in the ground and excited manifolds of the ^{87}Rb D$_2$ transition are computed and displayed respectively in Figs. 2.3 and 2.4. When $B = 0$, the m_F states are degenerate as the atom has no preferred orientation in space (quantisation axis). We see only the $F = 1, 2$ and $F = 0, 1, 2, 3$ branches of the ground and excited states and no additional splitting. As the field becomes non-zero, the magnetic field vector **B** establishes a quantisation axis, and the degeneracy of the m_F states is removed. This is seen in the splitting of the branches into individual sublevels.

The hyperfine linear Zeeman, intermediate, and hyperfine Paschen–Back regimes are clearly distinguished in both figures. In the low-field HLZ regime, the levels split linearly with B according to Eqn. 2.2.13. In the intermediate regime, the competition between $\hat{\mathcal{H}}_{\text{hfs}}$ and $\hat{\mathcal{H}}_{\text{B}}$ is manifested in the curvature of the lines. When the lines become linear again, we are said to have entered the HPB regime. At this point, $\hat{\mathcal{H}}_{\text{B}} \gg \hat{\mathcal{H}}_{\text{hfs}}$, so the states are no longer arranged by F and m_F and instead by J, m_J and I, m_I. By way of example, in Fig. 2.4, the magnetic sublevels in each F state set out degenerate with one another and later rearrange into an order defined by their m_J value. In groups of four, these states are ordered by $m_J = -3/2, -1/2, +1/2, +3/2$; and within each group by m_I which has values between $-3/2$ and $+3/2$.*

---

*To avoid repetition, and also because (as the reader shall see) the main experimental signal occurs on the ^{87}Rb D$_2$ line, the analysis for rubidium 85 is moved to Appendix A.
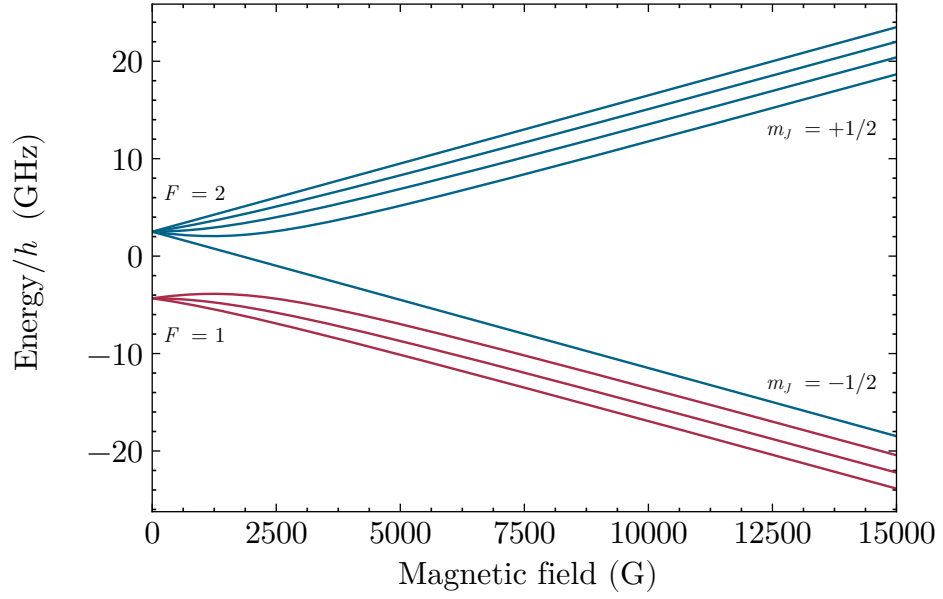
Figure 2.3 | Energy splitting of the ^{87}Rb 5^2S$_{1/2}$ state in the presence of an external magnetic field. The levels are grouped according to the value of F in the HLZ regime (< 100 G) and m_J, m_I in the HPB regime (> 4000 G). Figure generated with the ElecSus package in Python [35].

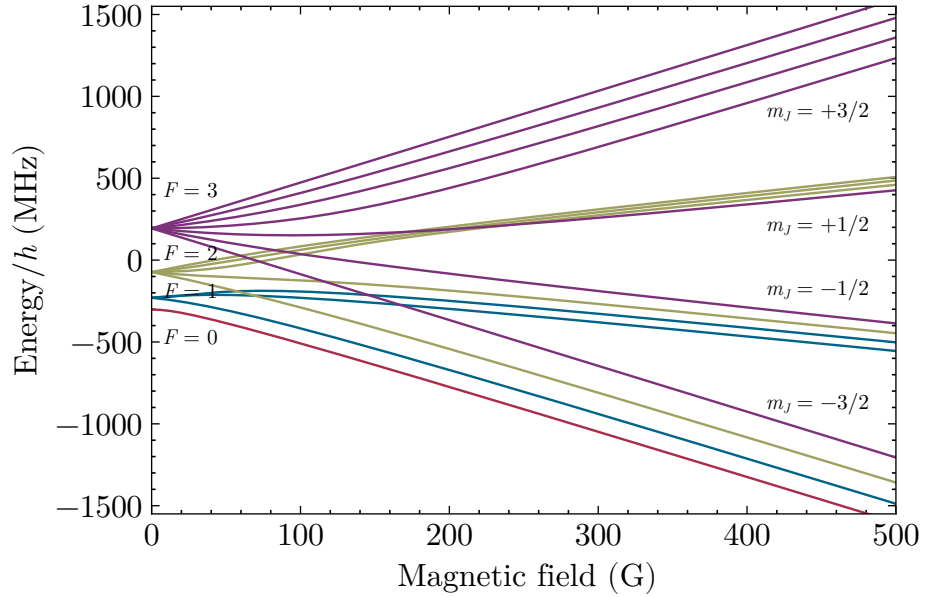**Figure 2.4 | The hyperfine splitting of the ^{87}Rb 5^2P$_{3/2}$ level in an applied magnetic field.** The levels are grouped according to the value of F in the HLZ regime and m_J, m_I in the HPB regime. Figure generated with the ElecSus package in Python [35].

2.2.3 Driving transitions

Not all transitions between atomic energy levels are allowed. Whether or not a transition can occur depends not only on the energy, but also on the conservation of momentum and angular momentum, as well as symmetry rules. Given two states $|n, L, m\rangle$ and $|n', L', m'\rangle$, the transition is said to be allowed where the transition dipole matrix element

$$\mathbf{d} = \langle n', L', m' | \hat{\mathbf{d}} | n, L, m \rangle \tag{2.2.15}$$

has at least one non-zero component

$$d_j = \langle n', L', m' | \hat{d}_j | n, L, m \rangle, \text{ with } j = x, y, z. \tag{2.2.16}$$

Evaluation of these integrals reveals that $d_j \neq 0$ only in those transitions where the change in the magnetic quantum number $\Delta m = 0, \pm 1$. Moreover, an electric dipole transition (which is the leading-order process in electronic transitions) demands that $\Delta L \pm 1$ and that the spin does not change, i.e. $\Delta S, \Delta I = 0$.

In the ^{87}Rb D$_2$ transition, $\Delta L = +1$. If the quantisation axis is taken to be along z, the following components of the radiative transition matrix element are non-zero:

$$\langle n, L+1, m+1 | \hat{d}_x + i\hat{d}_y | n, L, m \rangle, \text{ with } \Delta m = +1;$$

$$\langle n, L+1, m-1 | \hat{d}_x - i\hat{d}_y | n, L, m \rangle, \text{ with } \Delta m = -1;$$

and

$$\langle n, L+1, m | \hat{d}_z | n, L, m \rangle, \text{ with } \Delta m = 0.$$

Considering a dipole and its characteristics of absorption, the first two correspond to the case of two superimposed electric dipoles that are separated in phase by $\pi/2$ oscillating respectively in the x and y planes. This leads to the observation of a circularly-polarised electric field vector propagating along the z axis, which is to be matched by the polarisation of the driving field. Thus a σ^+ ($\Delta m = +1$) transition is driven by left-circularly polarised light, and a σ^- ($\Delta m = -1$) transition is driven by right-circularly polarised light. The third corresponds to that of a photon linearly-polarised along the z axis and propagating on any axis in the xy plane, with selection rule $\Delta m = 0$ on the atom.

In the absence of an external magnetic field, the magnetic sublevels of an atom are degenerate, so the $\sigma^{\pm}$ (and indeed the π) transitions have the same energy. As the B-field builds up, the sublevels in both the ground and excited manifolds will split, and the transitions are no longer identical in energy. Fig. 2.5(a) shows the dipole-allowed σ transitions for the ^{87}Rb D$_2$ line in a 4.7 kG magnetic field: here we are in the HPB regime, so the energy levels are labelled by the $m_{J,I}$ quantum numbers which dominate the atomic eigenstates, with selection rules $\Delta m_I = 0$ and $\Delta m_J = \pm 1$. The Zeeman shifts of the transitions are depicted in Figs. 2.5(b) and 2.6.
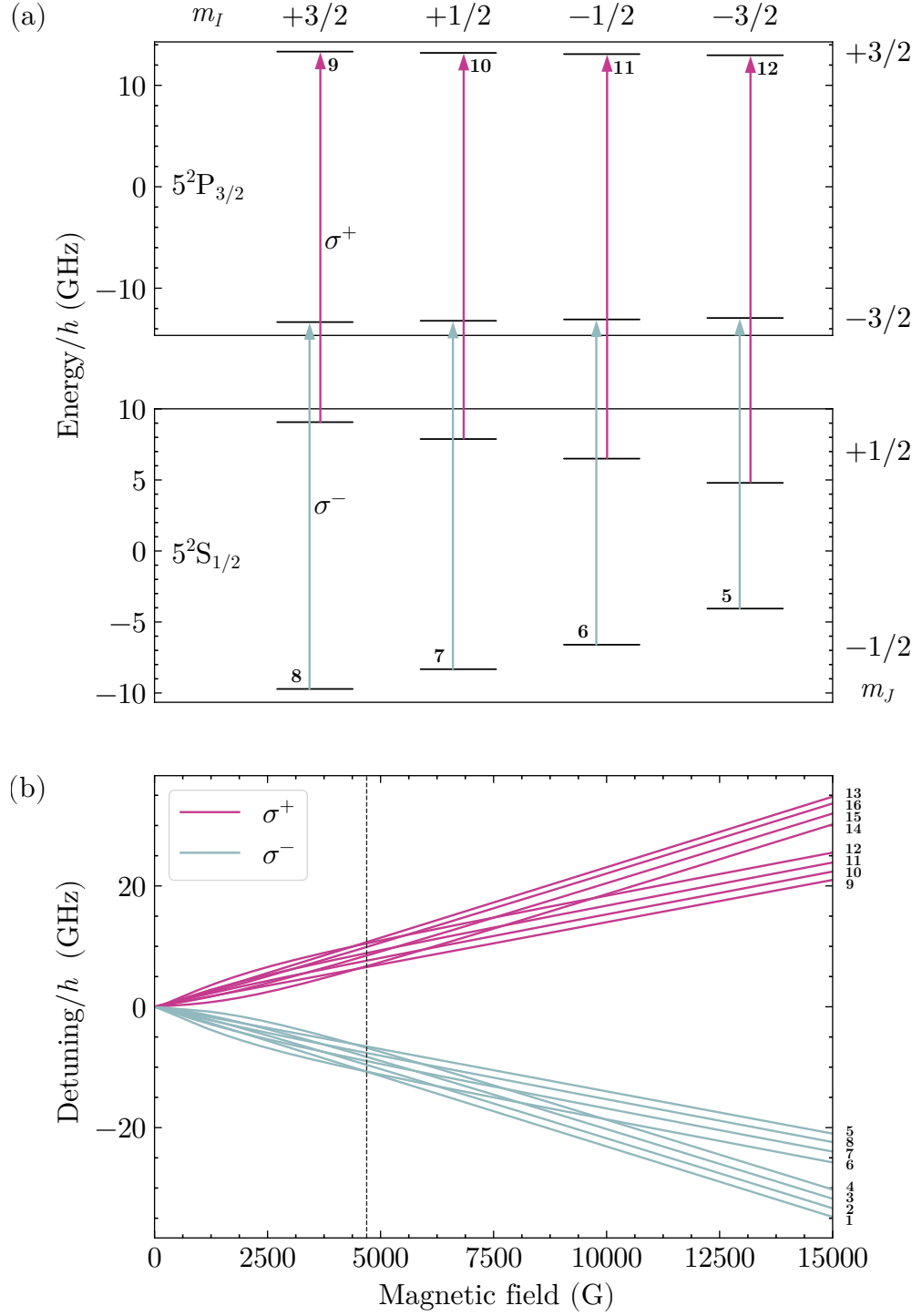
Figure 2.5 | (a) Optical pumping at 4.7 kG and (b) Zeeman shift of the ^{87}Rb D$_2$ transition for the absorption of σ^+ (pink) and σ^- (blue) light. In (a), the energy levels are distinguished by the m_J and m_I quantum numbers which dominate the atomic eigenstates in the HPB regime. The arrows (not drawn to scale) correspond to transition components 5–12 in Fig. 2.6. Notice that in (b) the detuning is plotted for the *transition energy* between two levels, rather than for individual levels.

2.3 Hypothesis

Our hypothesis is therefore this: knowing that an MTS error signal can be obtained for a closed atomic transition, and making use of the fact that the atomic energy levels shift in response to an external magnetic field (the Zeeman effect), we propose a scheme which combines the two components to allow the arbitrary relocation of an MTS error signal.
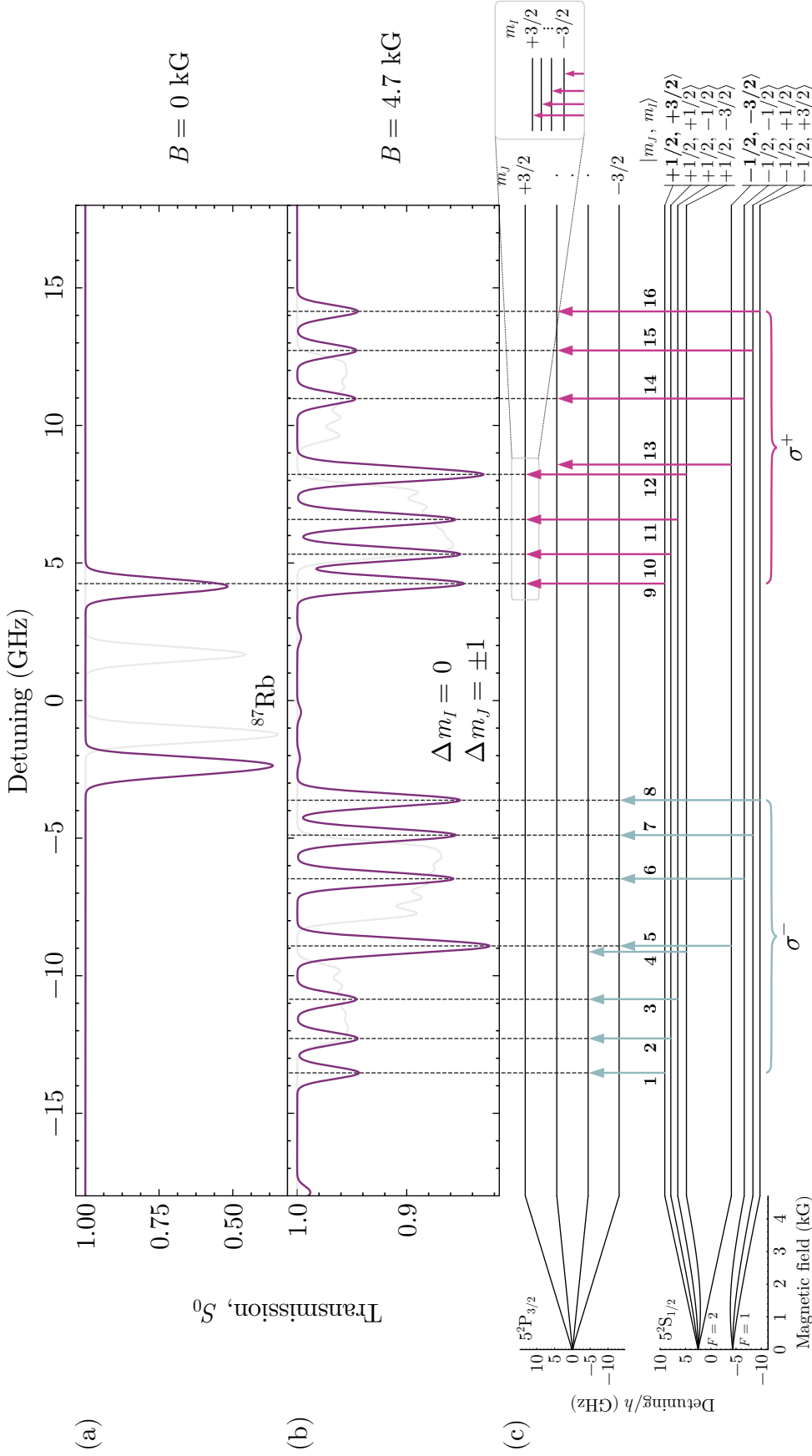
Figure 2.6 | Theoretical weak-probe spectra for the ^{87}Rb D$_2$ line at (a) $B = 0$ and (b) 4.7 kG with linear polarisation. In zero external B-field, (a), the two absorption lines correspond to the two hyperfine ground states $F = 1, 2$. The hyperfine transitions ($F \rightarrow F'$, $F \rightarrow F' - 1$, $F \rightarrow F' + 1$) are unresolved within each Doppler-broadened band. In (b) we are in the HPB regime, where nearly all transitions are resolvable and correspond to those indicated by the vertical arrows in the energy level diagram (c). The eigenstates of the system are labelled in the $|m_J, m_I\rangle$ basis with the basis state that dominates its composition at high magnetic fields, with the stretched states marked in bold. For reference, the ^{87}Rb spectra are shown in the background in grey. Produced with ElecSus in Python [35].

3 Experimental apparatus

3.1 Experimental setup

The experimental setup for Zeeman-tunable MTS (ZMTS) is illustrated in Fig. 3.1(a). The experiment uses an ultra-narrow linewidth MSquared SolsTiS laser to achieve the desired spectral range (15 GHz), but typical diode lasers may also be used in the case of a smaller range. 4.6 mW of 780 nm light is separated into pump (3.5 mW; $1/e^2$ radius 0.52 ± 0.01 mm) and probe (1.1 mW; $1/e^2$ radius 0.55 ± 0.01 mm) beams with a low-order half-wave plate and a polarising beamsplitter. The pump beam is phase modulated by an electro-optic modulator (Photonic Technologies EOM-02-12.5-V), driven below the resonant frequency at 8.5 MHz to prevent 'kinking' of the error signal [10]. To minimise the effects of residual amplitude modulation (RAM) [36], the polarisation of the incoming light can be adjusted via a half-wave plate before the EOM. A non-polarising beamsplitter is then used to reflect the pump and its accompanying sidebands into a 2 mm long vapour cell of natural abundance rubidium, where it interacts with the counterpropagating probe beam via the χ^3 susceptibility of the medium in a FWM process. The generated sideband, now induced onto the probe, beats with the carrier to produce an oscillating signal at the modulation frequency ω_m. This signal is detected on a fast photodiode (Hamamatsu C10508-01), amplified (Mini-Circuits ZFL-500), downmixed (Mini-Circuits ZX05-1L-S), and finally fed into a proportion-integration-differentiation (PID) controller (Toptica FALC 110) to output the MTS error signal. The relative phase shift between the modulation signal and the reference signal supplied to the mixer can be set digitally using a two-channel RF generator (Tektronix AFG 1062) with phased-matched outputs and variable offset.

This setup differs from conventional MTS [Fig. 3.1(b)] in that a large constant magnetic field is applied to the vapour cell along the axis of the propagating beams. This is provided by a pair of 'top hat'-shaped NdFeB magnets, as depicted in Fig. 3.1(a) in a cross-sectional view. Ideally, the magnetic field strength, and thus the position of the lock signal, can be varied easily by changing the separation between the magnets. The two quarter-wave plates on either side of the magnets serve to control the circularity, and more importantly the handedness, of the incoming pump and probe polarisations. This allows the selective driving of σ^+ and σ^- transitions with right- (RCP) and left-circularly polarised (LCP) light respectively, adding another level of tunability to the already versatile method. In the sections to come, each of these components shall be examined in turn.
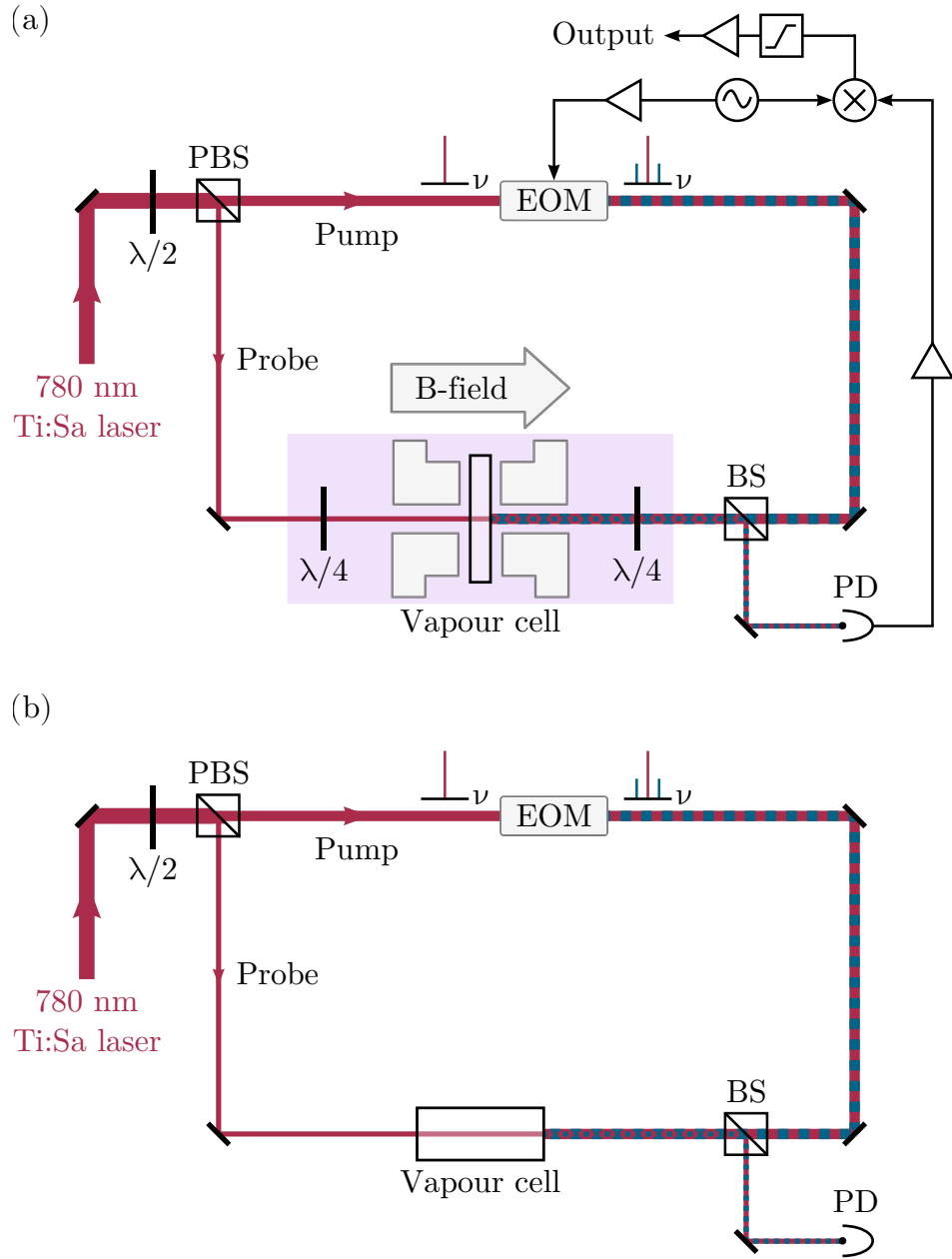
Figure 3.1 | Experimental setups for (a) Zeeman-tunable modulation transfer spectroscopy and (b) conventional modulation transfer spectroscopy, where $\lambda/2$ = half-wave plate, $\lambda/4$ = quarter-wave plate, BS = 50:50 non-polarising beamsplitter, EOM = electro-optic modulator, PBS = polarising beamsplitter, and PD = photodiode. The sideband-modulated pump and unmodulated probe beams are allowed to propagate collinearly through a heated rubidium cell of natural abundance and length 2 mm, across which a uniform magnetic field of up to 7 kG is applied. A half-wave plate can be placed in front of the EOM to reduce residual amplitude modulation effects. The shaded region highlights the main differences between the two schemes. The electronic signal lines are drawn here in black and are omitted in (b) for simplicity.

3.2 Vapour cell and heaters

3.2.1 2 mm vapour cell

Moderately large magnetic fields are necessary for the purposes of this investigation. In the current setup, field strengths of up to 7 kG are implemented using a pair of 'top-hat' NdFeB magnets. Though possessing the advantage of making large fields easily accessible, the small inter-magnet separations required for the permanent magnets to achieve such fields, and to achieve them homogeneously, necessitate very compact vapour cells.
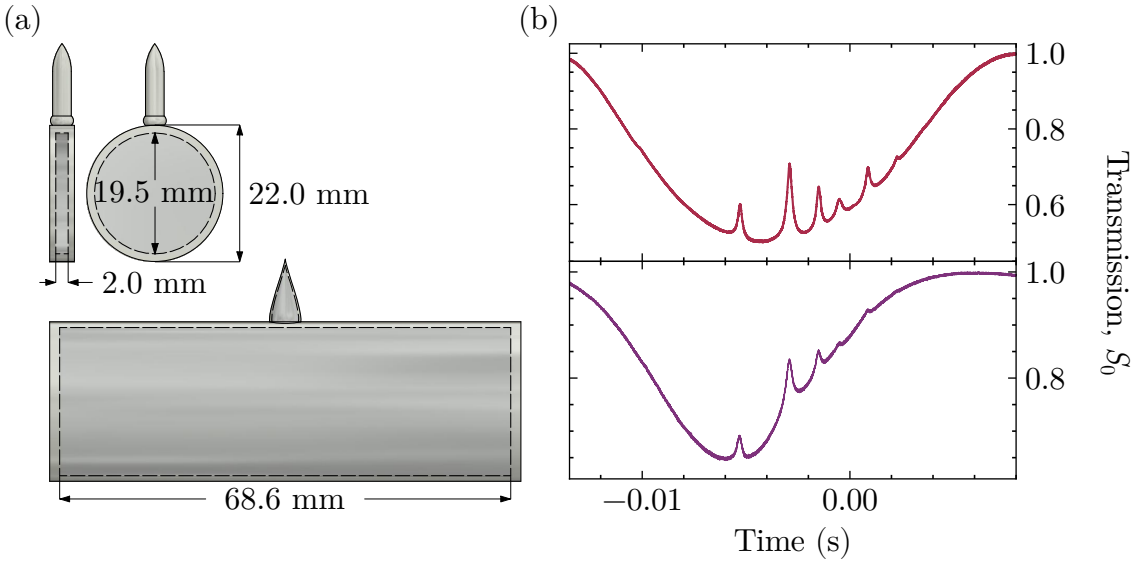

Figure 3.2 | Schematics of (top) the 2 mm Rb vapour cell used in the experiment and (bottom) a typical 70 mm-long cell, (a). The 2 mm cell consists of two parts: a glass window for optical access, and a vertical side-arm which acts as the rubidium metal reservoir. Shown in (b) are their respective saturated absorption spectra for the ^{87}Rb $F = 2 \rightarrow F' = 3$ cooling transition.

The dimensions of the 2 mm rubidium vapour cell used in the experiment are shown in Fig. 3.2(a). Containing rubidium in its natural abundance (72.15% ^{85}Rb; 27.85% ^{87}Rb) and fabricated from borosilicate glass, these reference cells are commercially available from Triad Technology. Without telescopes, the effective sub-Doppler linewidth of the ^{87}Rb $F = 2 \rightarrow F' = 3$ cooling transition is found to be 12.72 MHz.

3.2.2 Heater

At ambient conditions, the vapour in the 2 mm cell is optically thin and no absorption peaks are visible. This is overcome by Ohmic heating of the vapour cell to temperatures of around 125°C—see Fig. 3.2(b).

Figs. 3.3 and 3.4 show the ceramic heater (Thorlabs HT19R) and the mount designed for the heater-cell combination, respectively. Ceramic heaters are employed due

to their ability to endure high temperatures (up to 350°C), whereas the mount is 3D-printed from the heat-resistant and insulating polycarbonate (Ultimaker PC) material. The utilisation of 3D printing has rendered the fabrication process highly flexible, cost-effective and time-efficient. The body has room for a 2 mm vapour cell sandwiched by two ceramic heaters, and features a cut out for the stem of the cell and holes for optical access.
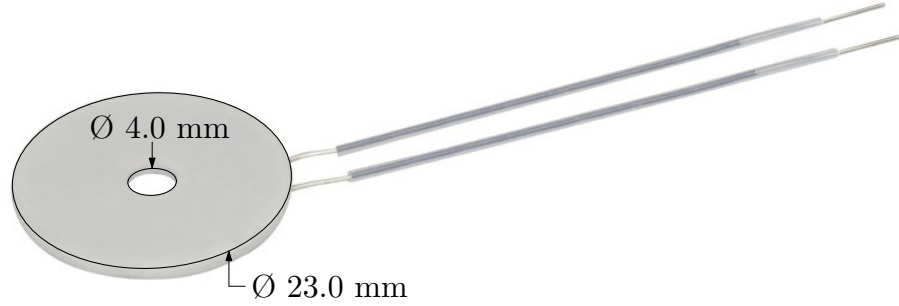
Figure 3.3 | Photograph showing the dimensions of the ceramic heater. One heater is placed either side of the vapour cell, heating it to ∼125°C to provide a sufficient optical depth for the probe.
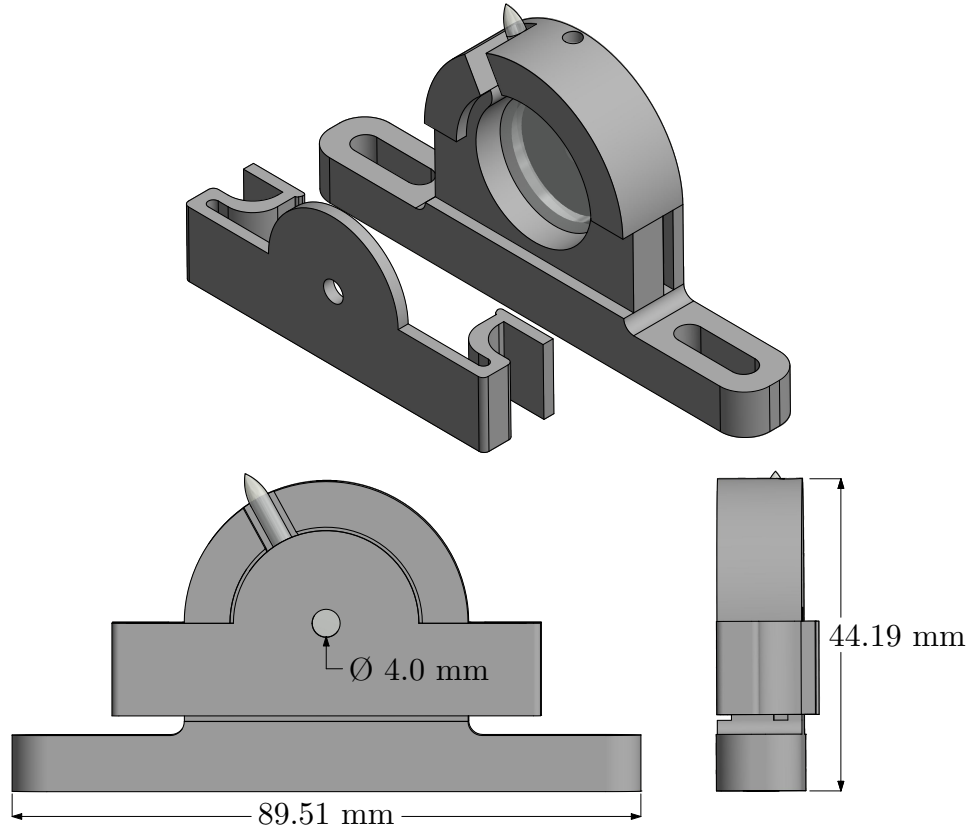
Figure 3.4 | Design for the 2 mm vapour cell mount employed in the experiment. The mount is 3D-printed from the Ultimaker PC filament and can withstand temperatures of up to 130°C. The stem of the cell sits in a carved-out slot, such that it is not directly heated and cooler than the cell windows. Holes with diameter 4.0 mm have been cut out to allow the laser beams to pass through.

3.3 Permanent magnets

The magnetic field B_z of a single annular magnet at position z_0 and along the axis of symmetry z can be described by the following formula:

$$B_z = \frac{B_0}{2} \left(\frac{z - z_0 + d}{\sqrt{(z - z_0 + d)^2 + R^2}} - \frac{z - z_0 - d}{\sqrt{(z - z_0 - d)^2 + R^2}} \right) \qquad (3.3.1)$$

where B_0 is the remanence of the magnet, and $2d$, R are the length and radius of the cylinder respectively. Since the magnetic field B too obeys the principle of superposition (in free space at least), the field for a ring magnet with outer radius R_o and inner radius R_i is just that from a cylinder of radius R_o deducted by the field from a cylinder of radius R_i. In the same way, the field profile of any magnetic material with cylindrical symmetry can be calculated.

The magnetic field in this experiment is generated using a pair of 'top hat'-shaped N52 grade NdFeB magnets [Fig. 3.6(a)], custom-made by and purchased from Shanghai Jinmagnets. Here we choose to work with permanent magnets over current-carrying solenoids for two main reasons, namely that no power is required, and that large fields are more easily accessible. The magnets are mounted on an aluminium block in threaded brass holders, which can be screwed in and out and thereby allow the achievement of different magnetic field strengths by varying the inter-magnet separation. A schematic of the magnets being held in the aluminium block is shown in Fig. 3.5.
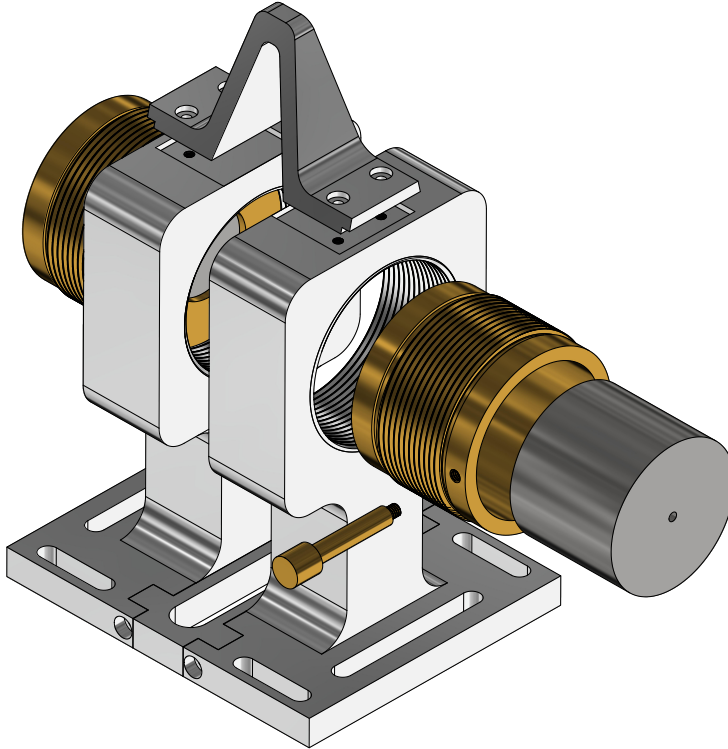
Figure 3.5 | Schematic of the aluminium magnet holder. The magnets can be screwed in and out with a lever.

(a)

(b)

(c)
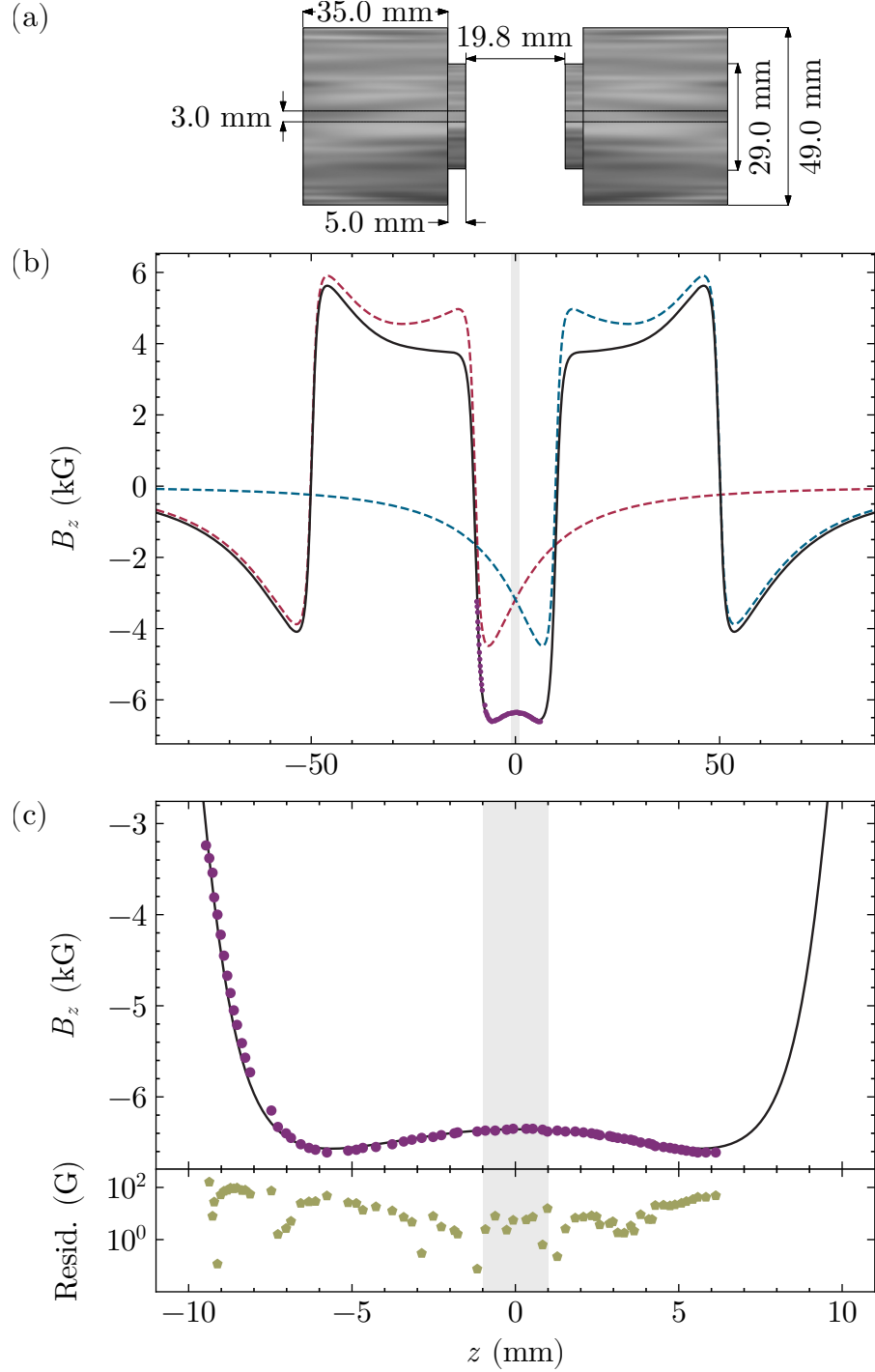
Figure 3.6 | Field profiles of the N52 grade NdFeB magnet pair in the axial direction, B_z. (a) Schematic of the 'top-hat' magnets, underneath which (b) the theoretical axial field profile (to scale with (a); shown in black) is plotted as a function of axial distance, z. The dashed red and blue lines display the field profile of each individual magnet. The purple circles signify Hall probe measurements, with error bars too small to be seen. The region normally occupied by atomic vapour is shaded in grey. (c) shows a zoomed-in view of the field profile between the magnets, along with the residuals. At this distance, the average magnetic field across the cell is 6.6 kG, with a peak-to-peak variation of smaller than 0.2% of the measured field.

Fig. 3.6(b) shows the field profile of the magnet pair in the axial direction, B_z. The axially polarised magnets are arranged in a Hemholtz geometry, such that the sum of the fields at $z = 0$ is constructive. At this separation, the magnetic field across the cell ($-1 \leq z \leq 1$; grey strip in the figure) is $6.4\,\text{kG}$, with a peak-to-peak variation of less than 0.2% of the measured field. This is verified experimentally with a Hall probe (results presented as purple dots). The slight difference between the calculated and observed profiles is attributed to the loss of magnetisation of the neodynium since production. The average B-field in the cell as a function of the distance between the magnets is given in Fig. 3.7.
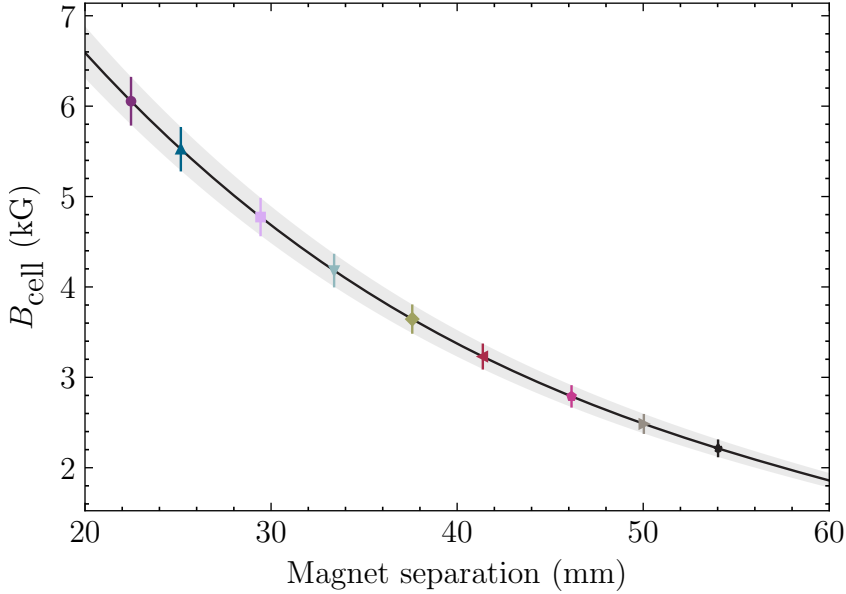

Figure 3.7 | **Average magnetic field strength in the 2 mm vapour cell, B_{cell}, as a function of magnet separation.** The calibration data is fitted to a cubic equation: $B_{\text{cell}} = -2.84 \times 10^{-5}s^3 + 5.54 \times 10^{-3}s^2 - 4.14 \times 10^{-1}s + 1.29$, with s being the magnet separation. The shaded region encloses possible values of the magnetic field within one error bar of the calibration curve. Data taken by D Carr for Ref. [37].

The field variation is an important quantity upon which the linewidth of the shifted transition is highly contingent. In this instance, the theoretically calculated field variation of 0.2% assumed that the vapour cell was positioned centrally between the two magnets, and that the magnets were separated by exactly $19.8\,\text{mm}$. In reality, however, the variation of the field depends strongly on both the position of the cell and the distance between the magnets. This is demonstrated more clearly in Fig. 3.8, where the root-mean-square (rms) and peak-to-peak (ptp) variations are visualised respectively in red and blue. In the case of the rms variation, we find from the theoretical model that the separation between the magnets must be set to $14.6 \pm 0.2\,\text{mm}$ to avoid additional line broadening. As for the positioning of the vapour cell, the variation within the cell, even when placed centrally, is above the upper limit at which the ^{87}Rb D$_2$ lines remain unbroadened. Clearly, the requirements become even more stringent if we consider instead the ptp variation. The effects of field inhomogeneity on the linewidth of the Zeeman-shifted transition will be examined in greater detail in Section 4.2.2.

Unshielded, the current setup has an axial leakage field that falls to that of the Earth's at a distance of 0.7 m [Fig. 3.9]. Further information regarding field uniformity and magnet design can be found on the Durham University Collections repository (doi:10.15128/r2r207tp335) as well as in Refs. [38–40].
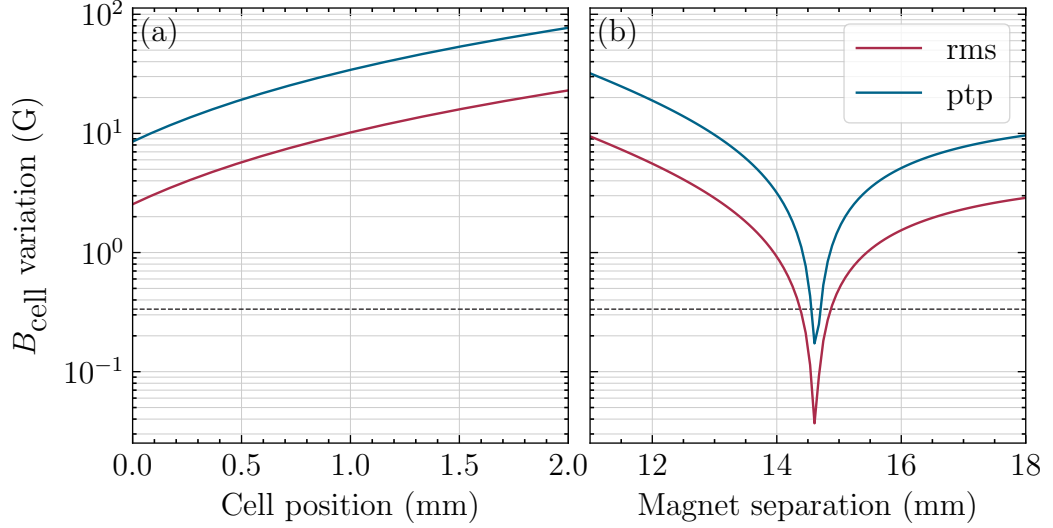
Figure 3.8 | The rms and ptp variation of the applied field as a function of (a) cell position and (b) magnet separation over the extent of the atomic vapour. The magnets are separated by 19.8 mm in (a). The dashed horizontal lines show the maximum variation the field can exhibit, at which the rubidium 87 D_2 σ-transitions remain unbroadened.
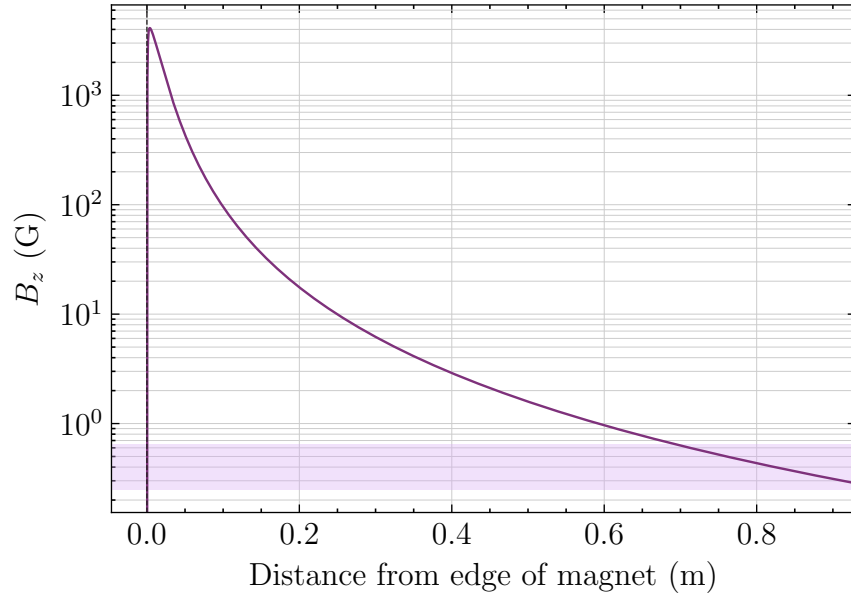
Figure 3.9 | Leakage field of the magnets in the axial direction when maximally wound out. From the edge of the magnet, this field falls to that of the Earth's (shaded in purple) at a distance of 0.7 m.

4 Zeeman-tunable modulation transfer spectroscopy

4.1 Experimental demonstration
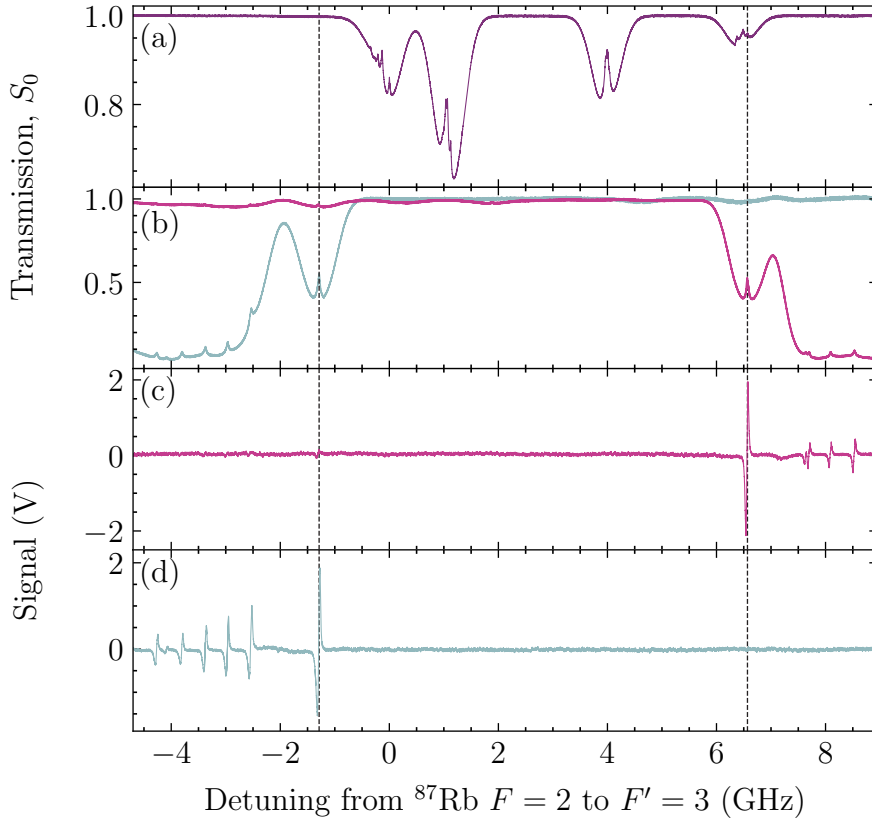
Figure 4.1 | First experimental demonstration of Zeeman-tunable modulation transfer spectroscopy. Doppler-free spectrum of the D_2 line in Rb vapour with (a) $B = 0$ and (b) $4.7\,\text{kG}$; and the ZMTS spectrum using (c) right- and (d) left-circularly polarised light. (c) shows the MTS error signal for the ^{87}Rb $F = 2 \to F' = 3$ cooling transition Zeeman-shifted onto the ^{87}Rb $F = 1 \to F' = 2$ repumping transition, and (d) vice versa. (c) and (d) are interchangeable by a 90°-rotation of the quarter-wave plates. The plethora of error signals in (c) and (d) is ascribed to contamination by ^{85}Rb. Colour: pink, with RCP incident light; blue, LCP.

Here we find confirmation of our initial hypothesis. The large applied magnetic field, in conjunction with the ability to select polarisations, support up to $\sim 10\,\text{GHz}$ of freedom in the error signal location (in practice, anywhere on the rubidium D_2 spectrum). To illustrate, Fig. 4.1 shows that by merely changing the helicity of the incident polarisation it is possible to select from lock points that are gigahertz apart. In particular, we show that the MTS error signal for the ^{87}Rb $F = 2 \to F' = 3$ cooling transition can be Zeeman-translated onto the ^{87}Rb $F = 1 \to F' = 2$ repumping transition (and vice versa) using a $4.7\,\text{kG}$ magnetic field, as well as how via a simple 90°-rotation of the quarter-wave plates, i.e. changing from RCP to LCP incident light, one might individually address the σ^+ and σ^- transitions.

Apart from the highlighted feature, we notice the plethora of smaller error signals in Figs. 4.1(c) and 4.1(d). We also note that, intriguingly, the main feature does not occur where the optical depth (OD) is greatest, even though intuitively one would expect the closed transition to give the highest OD. Both these observations are imputed to contamination by ^{85}Rb, which coexists with ^{87}Rb in natural abundance inside the vapour cell, and which renders the medium so optically thick in regions that the closed transitions become buried. A full breakdown of the observed features can be found in Section 4.2.1.
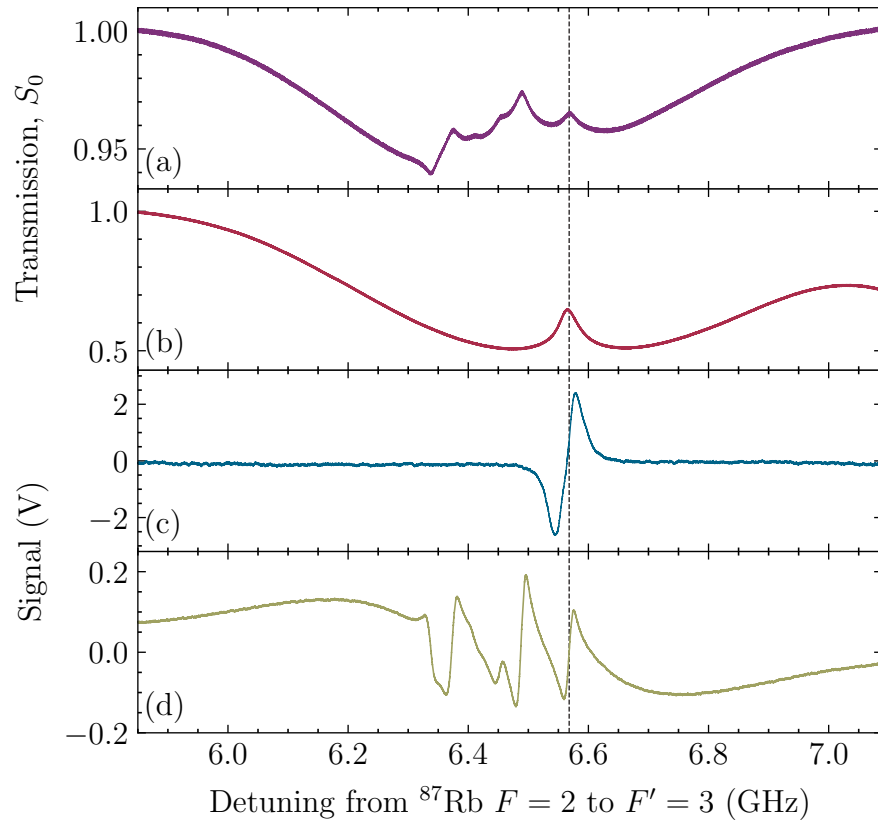

Figure 4.2 | A comparison between (c) ZMTS and (d) FMS for the ^{87}Rb $F = 1 \to F' = 2$ repumping transition. Also shown are the (a) normal and (b) Zeeman-shifted pump-probe spectra for the $F = 1 \to F'$ transitions. Note that the dip at $F = 1 \to F' = 0$ (leftmost in the first panel) is caused by optical pumping.

The form of the error signal, despite having been translated magnetically by $6.6\,\text{GHz}$ from the ^{87}Rb $F = 2 \rightarrow F' = 3$ cooling transition, is preserved. In stark contrast to that produced by the FMS technique, the dispersive lineshape sits on a flat, zero background that is unencumbered by residual linear-absorption effects, as is exemplified in Fig. 4.2(c). There is also the added advantage that only one dominant error signal is present on the spectrum, such that there is little ambiguity in the location of the lock-point—this allows a much more accurate determination of the spectral zero-point and, as a consequence, locking of the laser.

4.2 Comparison with theory

4.2.1 Detuning

To determine the experimental Zeeman-shift (detuning), the distance between the magnets is varied, and oscilloscope measurements of the error signal along with the reference spectrum are taken at each separation. Using the known frequency relation between the rubidium hyperfine peaks, the measurements are converted from time to frequency space. The detuning, then, is just the frequency shift in the error signal location from when $B = 0$.

Fig. 4.3 shows the frequency detuning of the ZMTS error signal with increasing magnetic field strength. As can be seen, the experimental detuning exhibits excellent accord with the theoretically predicted Zeeman-shift, enabling one to accurately predict the frequency shift simply by knowing the magnetic field. In agreement with our hypothesis, we identify the two main features to be due to, respectively, the ^{87}Rb $|-1/2, +3/2\rangle \rightarrow |-3/2, +3/2\rangle$ transition for σ^- (LCP) laser excitation, and ^{87}Rb $|+1/2, +3/2\rangle \rightarrow |+3/2, +3/2\rangle$ transition for σ^+ (RCP) laser excitation.* Represented in the present figure as solid black lines, these correspond to transition components 8 and 9 in Fig. 2.6. The rest of the spectral features are accounted for in full by the theory lines for the rubidium D_2 σ-transitions, shown in the figure as grey curves.

We note in passing that there also occurs a small amount of shifting due to the Earth's continuously changing magnetic field, but this shifting is on the order of $1\,\text{MHz}$ and is therefore negligible.

4.2.2 Linewidth

The MTS signal is related to the linewidth of the transition, Γ, via Eqn. 2.1.4. In view of this, it is important that consideration be given to the linewidth of the Zeeman-shifted transition, which affects not only the capture range but also the steepness of the lock signal.

As pictorialised in Fig. 4.4, the experimental linewidth is acquired firstly by fitting

---

*Here, and for the remainder of this thesis, we shall write our eigenstates in the $|m_J, m_I\rangle$ basis. Without exception, all transitions will be from $5S_{1/2} \rightarrow 5P_{3/2}$.
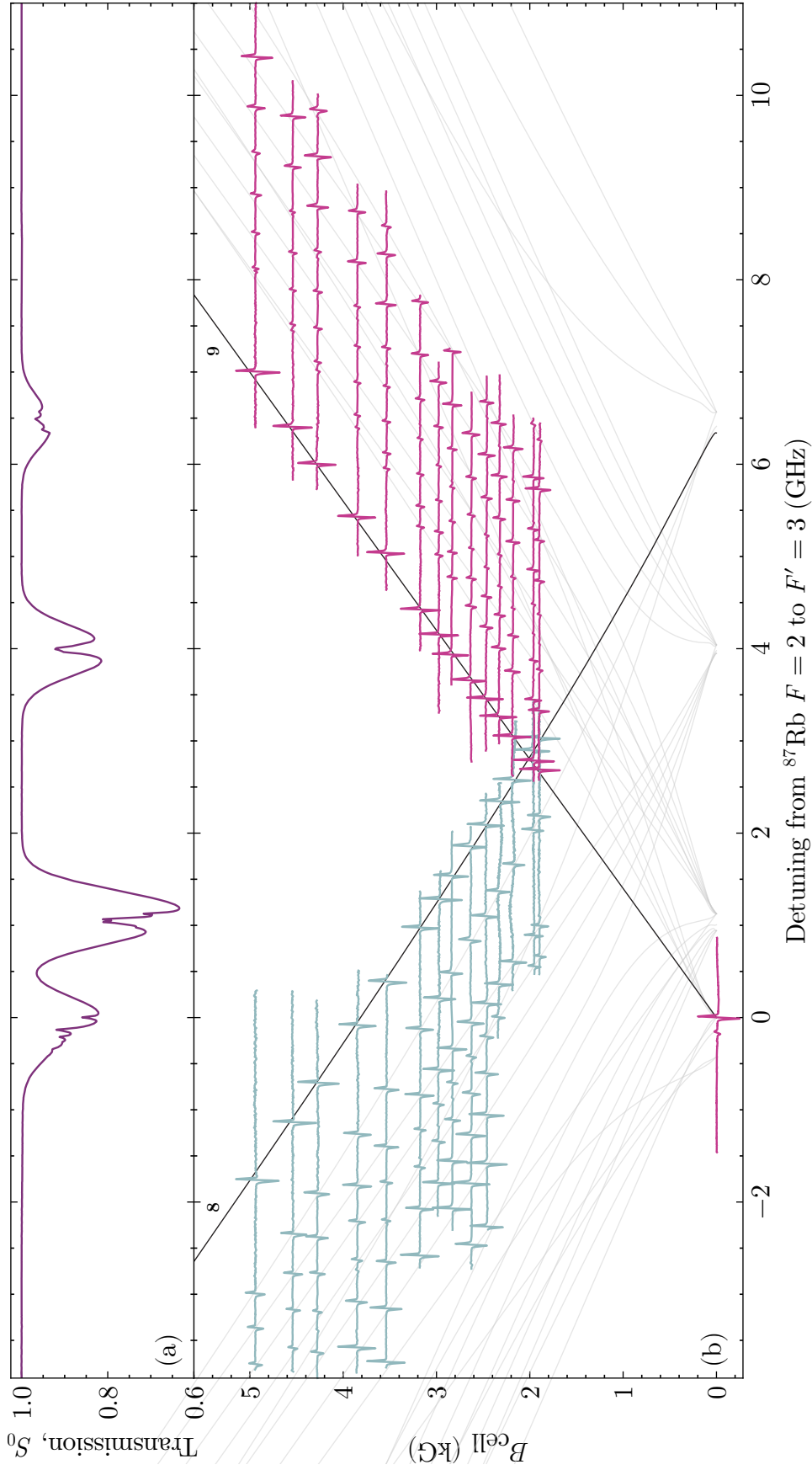
Figure 4.3 | Frequency detuning of the ZMTS error signals as a function of magnetic field strength, (b). Experimental traces of the error signal, driven respectively with σ^+ and σ^- light, are shown in pink and blue. The grey and black lines represent the theoretically predicted Zeeman-shifts of the rubidium D_2 σ-transitions, with the black lines accounting for the ^{87}Rb $|-1/2, +3/2\rangle \rightarrow |-3/2, +3/2\rangle$ (σ^-) and ^{87}Rb $|+1/2, +3/2\rangle \rightarrow |+3/2, +3/2\rangle$ (σ^+) transitions. The saturated absorption/hyperfine pumping spectrum for natural abundance rubidium (a) is included herein as a frequency reference. Note that in this instance the independent variable, being the magnetic field, is plotted on the y-axis for better clarity.

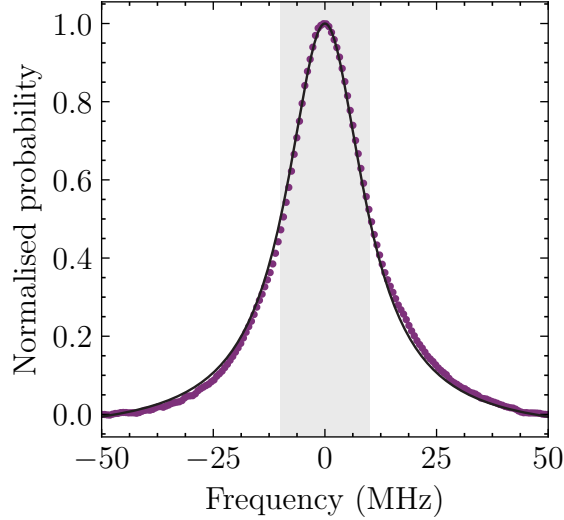**Figure 4.4 | Determination of the linewidth of the Zeeman-shifted transition.** The full width at half maximum (grey shaded region) of the fit Lorentzian (black) is taken to be the homogeneous linewidth of the transition.

a Lorentzian profile over the Zeeman-shifted saturated absorption feature, from which the full width at half maximum is then extracted. The theoretical linewidth, on the other hand, is obtained by taking into account the Zeeman-broadening arising from the magnetic field variation within the cell, and convolution of the resultant frequency distribution with the natural linewidth of rubidium [Fig. 4.5].

Though following the general trend of theory, the experimental linewidths (red circles in Fig. 4.6) are noted to be significantly higher than predictions of the theoretical lineshape model ($\Gamma = 6.065$ MHz; blue). The breakdown of the model at weaker fields, despite the absence of Zeeman-broadening (e.g. at $B = 0$ where the measured linewidth is 12.72 MHz), is suggestive of the fact that alternative broadening mechanisms—namely, power [41, 42] and transit-time broadening [43–46]—are in play. Convolving instead with this linewidth, fairly good agreement is found between the observed and calculated linewidths at high magnetic field strengths (> 4 kG). More work remains to be done to ascertain the source(s) of departure from theory at smaller fields.

4.2.2.1 Power broadening

Consider a two-level atom interacting with a steady light source. At any given time, the atomic populations are governed by the steady-state equilibrium between cw radiative excitation and various decay processes such as spontaneous emission and collisional relaxation. The experimentally observed signal (which has a Lorentzian dependence on Δ), S_{steady}, is then related to the excited state population $\langle P_2 \rangle$ by [47]

$$S_{\text{steady}} \propto \langle P_2 \rangle = \frac{1}{2} \frac{(I/I_{\text{sat}})}{1 + (\Delta/\beta)^2 + (I/I_{\text{sat}})}. \tag{4.2.1}$$

where $\Delta = \omega_0 - \omega$ is the detuning of the laser with respect to the atomic Bohr

29
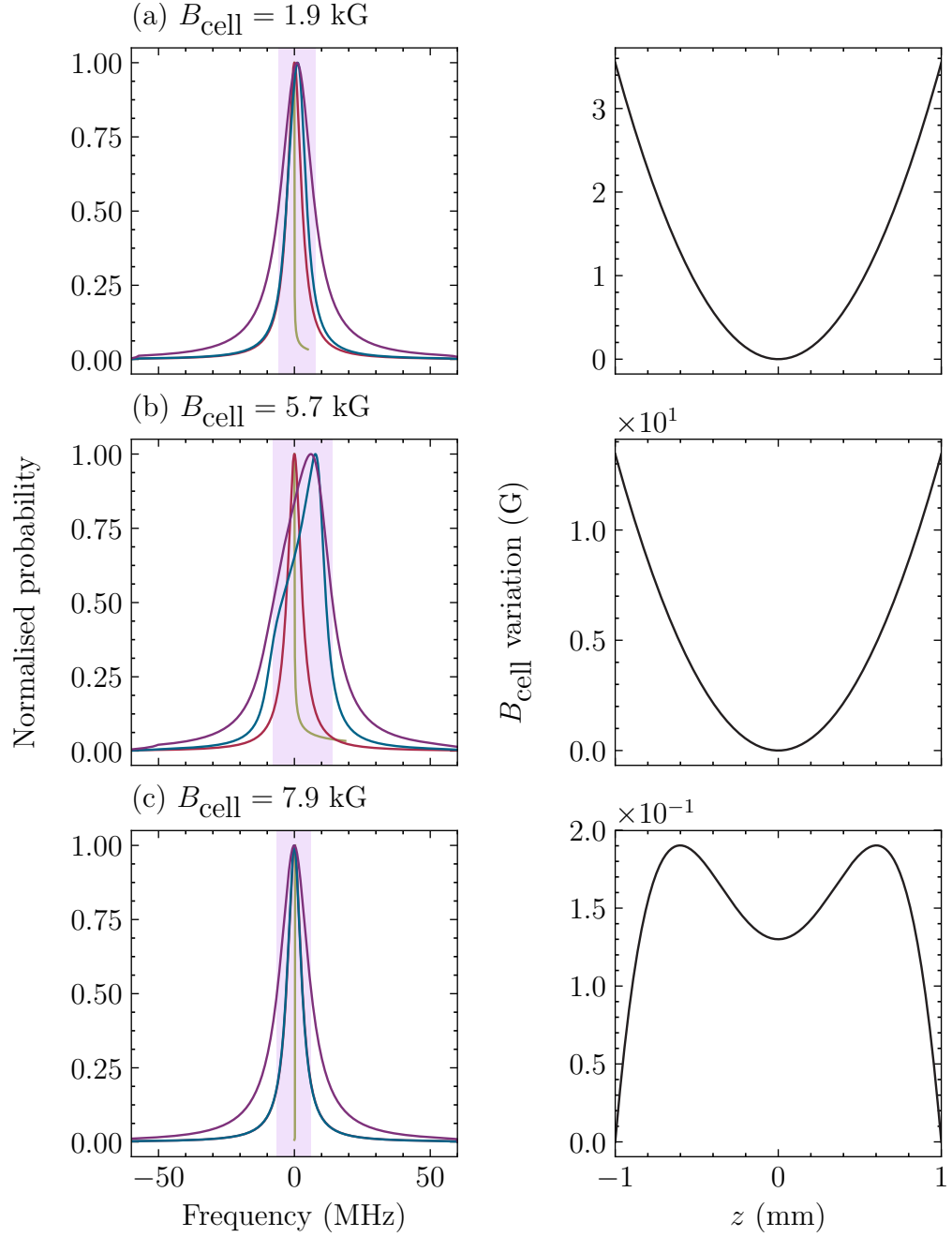
Figure 4.5 | Theoretical broadening of the ^{87}Rb $5S_{1/2}\,|+1/2, +3/2\rangle \rightarrow 5P_{3/2}\,|+3/2, +3/2\rangle$ transition (left), and variation of the magnetic field within the vapour cell (right) at (a) $B = 1.9\,\text{kG}$, (b) $5.7\,\text{kG}$, and (c) $7.9\,\text{kG}$. The theoretical lineshape (blue) is obtained via linear convolution of a Lorentzian lineshape with full half-width $6.065\,\text{MHz}$ (red; representative of the natural linewidth of rubidium) with the frequency distribution arising from inhomogeneities in the local field (olive). The purple lineshape is similarly obtained, convolving instead with $\Gamma = 12.72\,\text{MHz}$, the effective sub-Doppler linewidth in the $2\,\text{mm}$ cell. The theoretical linewidth (light purple strip) is taken to be the FWHM of the purple profile.
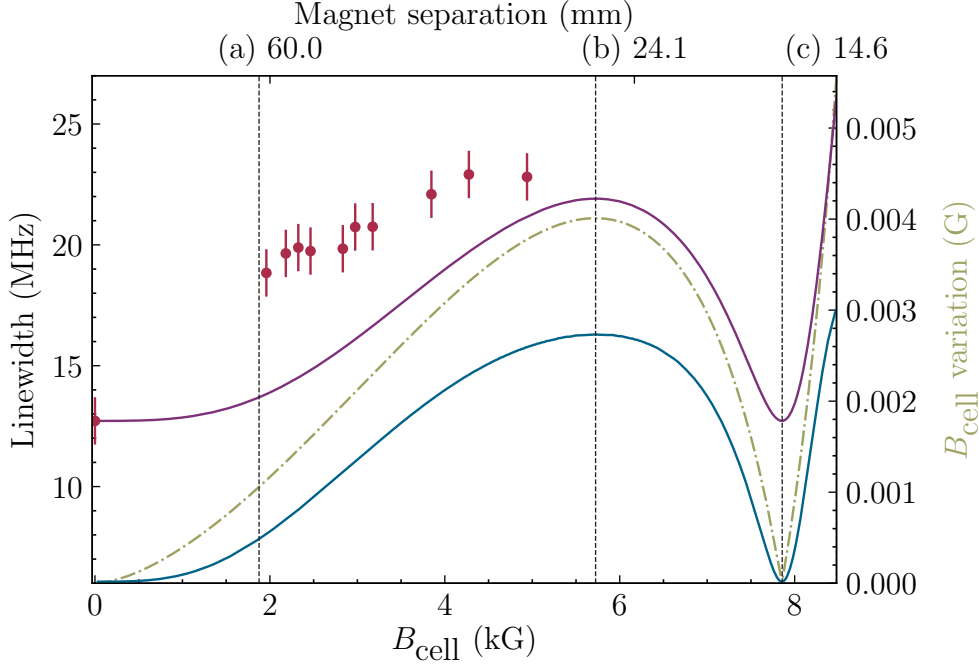
Figure 4.6 | Experimental (red circles) versus theoretical linewidth of the ^{87}Rb $5S_{1/2}\,|+1/2,+3/2\rangle \rightarrow 5P_{3/2}\,|+3/2,+3/2\rangle$ transition. The theoretical linewidths are computed by convolving the magnetic field distribution in the 2 mm cell with, respectively, Lorentzian profiles of full-halfwidths 12.72 MHz (purple) and 6.065 MHz (blue). The dashed black lines correspond to the B-fields at which (a) the magnets are maximally wound out [Fig. 4.5(a)], (b) the field variation reaches a local maximum [Fig. 4.5(b)], and (c) the field variation reaches a local minimum [Fig. 4.5(c)]. The olive dash-dotted line shows the magnetic field variation with increasing field strength.

frequency ω_0, β is some width parameter, and I_{sat} is the characteristic intensity at which the rate of stimulated emission is equal to that of spontaneous emission.

Eqn. 4.2.1 represents a conventional view of *power broadening*: an increase in the driving intensity I is expected to broaden the width of the Lorentzian line profile. This is because, as the radiation field becomes more intense, the atomic population oscillates faster between the two levels (though never spending more than half the time in each). Intuitively, this can be understood from Heisenberg's uncertainty principle which states that

$$\Delta\tau\Delta\epsilon = \hbar/2 \qquad\qquad (4.2.2)$$

Here, the uncertainty in the energy of the excited state $\Delta\epsilon$ is determined predominantly by its spontaneous lifetime ($\Delta\tau \approx \tau_0$). Hence the increased Rabi frequency, which can be thought of as the excitation and de-excitation having 'less time', will lead to a larger $\Delta\epsilon$. In a spectroscopic measurement, this is manifested in the broadening of a spectral line.[†]

[†]When all is said and done, however, the intensity dependence of the sub-Doppler linewidth in (Zeeman-tunable) modulation transfer spectroscopy is not trivial to calculate. Eqn. 4.2.1 assumes a simple two-level system which the four-wave mixing process intrinsically is not.

4.2.2.2 Transit-time broadening

If the interaction time of an atom with a driving field τ_{tt} is small relative to the spontaneous lifetime of the excited state, the linewidth of the sub-Doppler transition is not anymore limited by the spontaneous transition probabilities, but by the transit-time through the radiation field (in this case the laser beam). This effect is known as *transit-time broadening*.

An analogy can be drawn between excitations in an atom and a forced harmonic oscillator, in that the oscillator amplitude is proportional to the that of the driving field. Thus an atom traversing a laser beam with a Gaussian intensity profile $E = E_0 \exp(-r^2/w^2)\cos\omega t$ will have amplitude $x = x_0 \exp(-r^2/w^2)\cos\omega t$, where w is the waist of the Gaussian beam profile. Fourier transformation of the temporal signal yields [48]

$$I(\omega) = I_0 \exp\big(-(w-w_0)^2 \frac{w^2}{2v^2}\big), \qquad (4.2.3)$$

with a transit-time limited FWHM

$$\delta\omega_{tt} = 2(v/w)\sqrt{2\ln 2}, \qquad (4.2.4)$$

which is inversely proportional to τ_{tt}. Once more, this can be understood in terms of the mathematical uncertainty principle for Fourier transformations.

How such broadening effects may be circumvented will be discussed in Section 5.1.1. We acknowledge the presence of additional broadening due to collisional interactions with the background gases. Nevertheless, this buffer gas broadening affects the linewidth at all magnetic fields equally and so will not be covered here in depth.

4.3 Long-term stability

The frequency of a laser, even that which is locked, drifts around—this is why we needed an error signal in the first place. A lock is considered 'good' if the following can be said about it: i) the amplitude of the frequency oscillation is small compared to the natural linewidth of the transition, and ii) this oscillation remains small for a demonstrable amount of time.

To evaluate the long-term stability of our method, the overlapping Allan deviation [49, 50] of the beat note frequency between the ZMTS-locked laser (Toptica DL Pro) and an independent, MTS-stabilised laser was measured over a period of 24 hours. The laser remains locked for the entirety of this duration and exhibits frequency fluctuations well below the natural linewidth of the atomic transition (6.065 MHz), as can be seen from Fig. 4.7 which shows a *combined* frequency instability of < 1 MHz for the two lasers over times up to 10^3 s. The larger deviations at $\tau \sim 1$ s is thought to have originated from the unoptimised PID control; whereas the longer-term deprecation ($\tau > 10^4$ s) is attributed to drifts in ambient temperature.

The combined coherence time of the two lasers, which is the time for which their beat note frequency stays in phase, is found to be 0.33 μs [Fig. 4.8]. That being

said, we notice in a setup with two lasers that drifts in either destroys the coherence. So, unless they always drift in the same direction *and* for the same amount, the coherence time for a single, ZMTS-stabilised laser is almost certainly better than the stated value.

The demonstrated stability is sufficiently good for various applications such as laser cooling and, if required, could be further improved by incorporating the intensity stabilisation method discussed in Ref. [23].
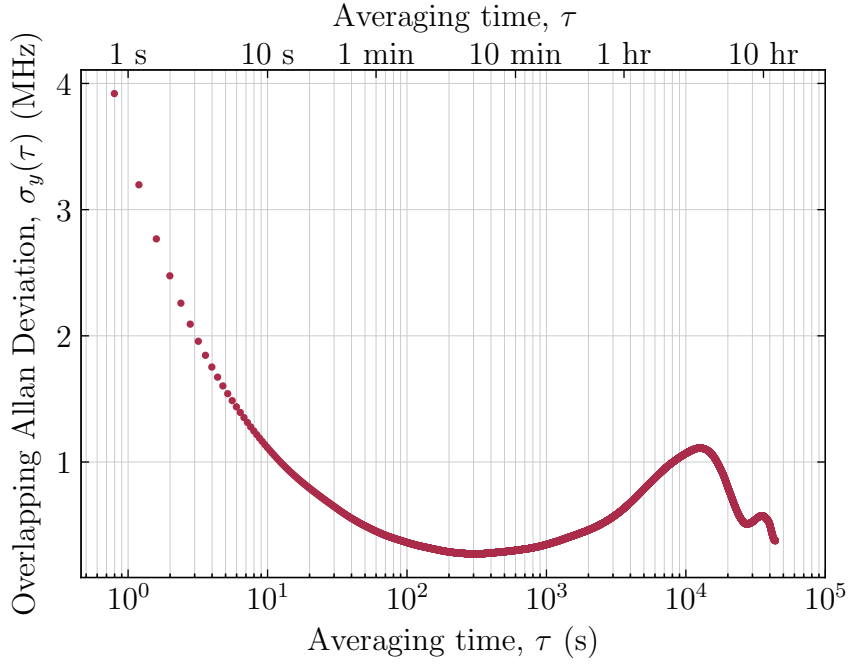

Figure 4.7 | Overlapping Allan deviation of the beat note frequency between the locked laser and a separate, MTS-stabilised laser.
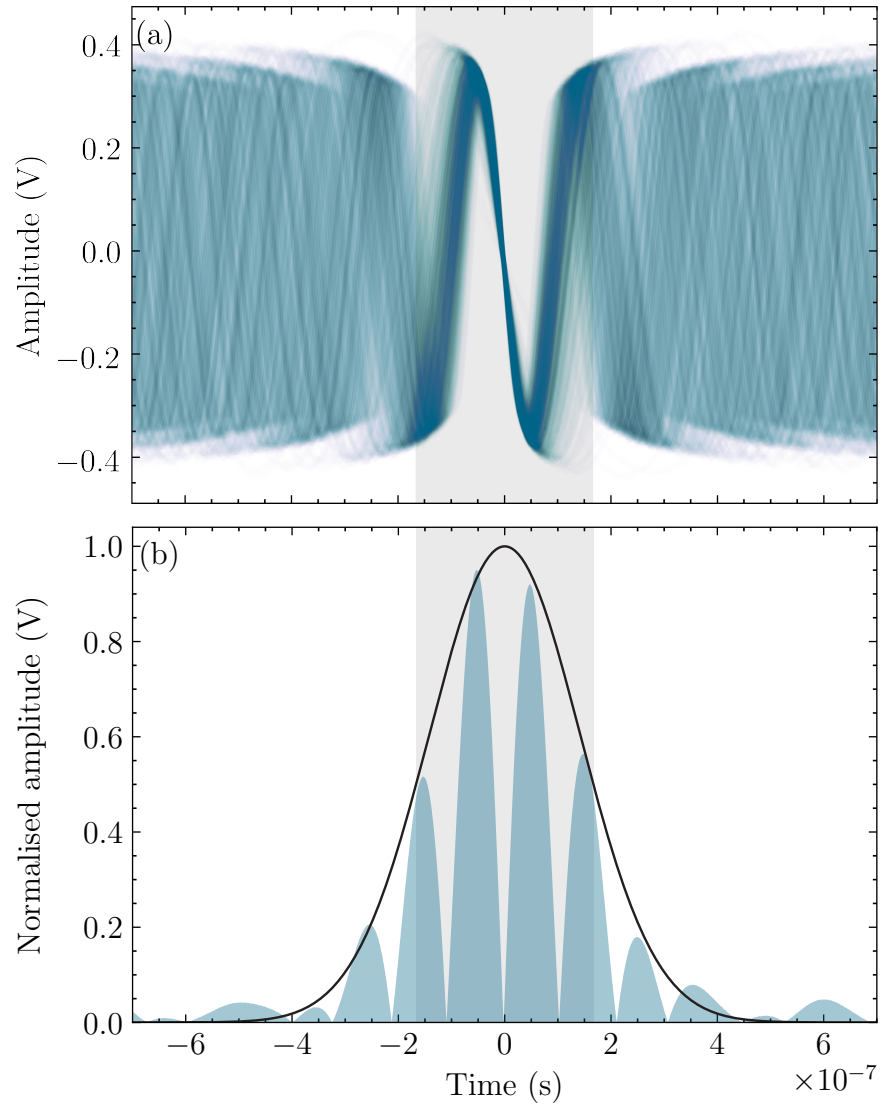
Figure 4.8 | Coherence of the beat note produced by two lasers, stabilised respectively with ZMTS and MTS. The two figures here aim to convey the same information: in (a), the coherence is shown with colour transparency (determined by the alpha parameter), by overlaying 1000 shots of the beat signal with low alpha in a 'persistence'-type plot. In (b), the same is displayed, but this time with amplitude by summing over the different shots. The combined coherence time of the two lasers, which is the FWHM of the approximately Gaussian envelope of the beat (shaded in grey), is found to be $0.33\,\mu s$.

5 Outlook and Conclusion

5.1 Outlook

5.1.1 Scope for future work

As have been alluded to above, the biggest drawback of the ZMTS technique lies in the linewidth, or the broadening thereof, of the Zeeman-shifted transition. From Fig. 4.5 it is apparent that different effects contribute to the observed broadening in different regimes.

At low magnetic field strengths, power and transit-time broadening are the dominant broadening pathways (see Sections 4.2.2.1 and 4.2.2.2). These deficits can easily be reversed by the use of telescopes, which enlarge the laser beams to have the effect of decreasing the intensity and increasing the time of flight [Fig. 5.1].
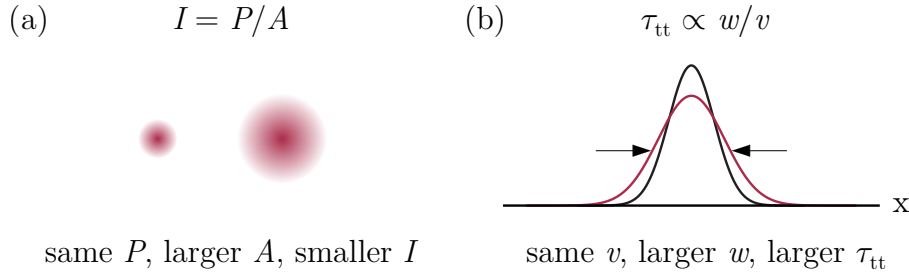

(a) $I = P/A$ (b) $\tau_{tt} \propto w/v$

same P, larger A, smaller I same v, larger w, larger τ_{tt}

Figure 5.1 | Effect of the telescope on (a) power broadening and (b) transit-time broadening. In the case of power broadening, since the intensity is the power per unit area ($I = P/A$), and magnifying the beam does not change the source power, adding the telescope serves to decrease I by increasing A. In the case of transit-time broadening, the transit-time limited halfwidth, $\delta\omega_{tt}$, is inversely proportional to the laser beam waist (ω). Hence the use of telescopes, which increases ω, reduces the broadening.

Zeeman-broadening, on the other hand, becomes the primary broadening channel at large B. Contrary to the low-field case, this broadening is technical in nature: the non-uniformity of the magnetic field, with which the spectral width of the transition line increases, stems from fundamental flaws in the magnet design. Ideally, this could be solved by redesigning the magnets; alas, we find in actuality that achieving with permanent magnets a homogeneous field over the interested range is highly challenging. A viable alternative is to use a solenoid, which produces a nearly

uniform field at the core. Nevertheless, this comes at the expense of the portability and relative ease of use offered by the current setup. Yet another improvement that can be made to the setup involves the motorisation of the magnet holder. This permits a more precise tuning of the separation between the magnets, which in turn controls both the homogeneity and strength of the magnetic field.

Moving away from considerations of the linewidth, a penultimate suggestion would be to increase the range over which the magnet separation is tunable. At present, the largest separation achievable with the setup is 60.0 mm, equalling a smallest attainable field of 1.8 kG and ~ 2.5 GHz detuning in the main error signal's location. Doubling this distance reduces the magnetic field experienced by the vapour cell by a further magnitude, to 0.5 kG which corresponds to a Zeeman-shift of ~ 0.7 GHz.

Finally, we register that elements of the experiment such as the magneto-optical trap and optical molasses may be sensitive to the large, stray magnetic field. However, this can easily be resolved by mu-metal shielding the magnets or, alternatively, by fibre-coupling the ZMTS setup.

5.1.2   Applications

Though demonstrated here in the context of rubidium, the ZMTS method can be conveniently extended to other atomic and molecular species. Indeed, the method might even find use in the trapping of the different isotopes of an element.

We note that the following is better implemented in a solenoid system, but a useful implication of this Zeeman-tunability is that the frequency of the *locked* laser can be changed simply by changing the magnetic field. To put simply, a lock with a tunable bandwidth can be achieved by sending an alternating current to the electromagnet, assuming the laser PZT is able to keep up. In principle, this can be used to address and trap the different isotopes in a multi-isotope magneto-optical trap.

Where ZMTS is most apt, still, is when the laser has to be locked to some fixed frequency detuning from an absorption line, e.g. in Raman and lattice lasers. These form a fundamental building block of any AMO physics experiment, and as such we expect our technique to find widespread applications in laser spectroscopy, laser cooling and trapping, and precision measurement with atoms and lasers [51–53].

5.2   Conclusion

Active frequency stabilisation of a laser is paramount to many areas of research. On account of its zero background and excellent signal-to-noise ratio, modulation transfer spectroscopy has emerged as one of the most robust and widely employed laser locking techniques. For all its virtues, the four-wave mixing process which underlies MTS means that the observation of strong modulation transfer signals only occurs at closed transitions, precluding MTS from numerous use cases.

Improving upon the existing MTS scheme, we present in this thesis a technique

to magnetically translate the spectral location of an MTS error signal by simple application of a large axial magnetic field. Retaining all of the advantages of MTS, the proposed scheme generates ideal error signals based on stable atomic references, with the additional benefits of being highly tunable and reproducible. Limited only by the strength and homogeneity of the applied field, we show that the error signal for the ^{87}Rb $F = 2 \rightarrow F' = 3$ cooling transition can be arbitrarily shifted on the D$_2$ spectrum, including onto the the ^{87}Rb $F = 1 \rightarrow F' = 2$ repumping transition. Excellent agreement is found between experiment and theory.

Locking the laser to the shifted signal gives a frequency stability of better than $1\,\text{MHz}$ for timescales up to $10^3\,\text{s}$. While the technique was demonstrated in the context of the ^{87}Rb D$_2$ line, the same method can be conveniently extended to other atomic species and types of lasers (e.g. Raman and lattice lasers).

Bibliography

[1] K. L. Corwin, Z.-T. Lu, C. F. Hand, R. J. Epstein, and C. E. Wieman, 'Frequency-stabilized diode laser with the Zeeman-shift in an atomic vapor,' Applied Optics **37**, 3295–3298 (1998).

[2] A. Millett-Sikking, I. G. Hughes, P. Tierney, and S. L. Cornish, 'DAVLL lineshapes in atomic rubidium,' Journal of Physics B: Atomic, Molecular and Optical Physics **40**, 187–198 (2006).

[3] D. J. McCarron, I. G. Hughes, P. Tierney, and S. L. Cornish, 'A heated vapor cell unit for dichroic atomic vapor laser lock in atomic rubidium,' Review of Scientific Instruments **78**, 093106 (2007).

[4] D. W. Preston, 'Doppler-free saturated absorption: laser spectroscopy,' American Journal of Physics **64**, 1432–1436 (1996).

[5] C. Wieman and T. W. Hänsch, 'Doppler-free laser polarization spectroscopy,' Physical Review Letters **36**, 1170–1173 (1976).

[6] C. P. Pearman, C. S. Adams, S. G. Cox, P. F. Griffin, D. A. Smith, and I. G. Hughes, 'Polarization spectroscopy of a closed atomic transition: applications to laser frequency locking,' Journal of Physics B: Atomic, Molecular and Optical Physics **35**, 5141–5151 (2002).

[7] G. C. Bjorklund, 'Frequency-modulation spectroscopy: a new method for measuring weak absorptions and dispersions,' Optics Letters **5**, 15–17 (1980).

[8] J. H. Shirley, 'Modulation transfer processes in optical heterodyne saturation spectroscopy,' Optics Letters **7**, 537–539 (1982).

[9] J. Zhang, D. Wei, C. Xie, and K. Peng, 'Characteristics of absorption and dispersion for rubidium D_2 lines with the modulation transfer spectrum,' Optics Express **11**, 1338–1344 (2003).

[10] D. J. McCarron, S. A. King, and S. L. Cornish, 'Modulation transfer spectroscopy in atomic rubidium,' Measurement Science and Technology **19**, 105601 (2008).

[11] B. A. Olsen, B. Patton, Y.-Y. Jau, and W. Happer, 'Optical pumping and spectroscopy of Cs vapor at high magnetic field,' Physical Review A **84**, 063410 (2011).

[12] A. Sargsyan, G. Hakhumyan, C. Leroy, Y. Pashayan-Leroy, A. Papoyan, D. Sarkisyan, and M. Auzinsh, 'Hyperfine Paschen–Back regime in alkali metal

atoms: consistency of two theoretical considerations and experiment,' JOSA B **31**, 1046–1053 (2014).

[13] A. Sargsyan, A. Tonoyan, G. Hakhumyan, C. Leroy, Y. Pashayan-Leroy, and D. Sarkisyan, 'Complete hyperfine Paschen–Back regime at relatively small magnetic fields realized in potassium nano-cell,' EPL (Europhysics Letters) **110**, 23001 (2015).

[14] A. D. Sargsyan, G. T. Hakhumyan, A. H. Amiryan, C. Leroy, H. S. Sarkisyan, and D. H. Sarkisyan, 'Atomic transitions of Cs D_2 line in strong transverse magnetic fields,' Journal of Contemporary Physics (Armenian Academy of Sciences) **50**, 317–326 (2015).

[15] A. Sargsyan, E. Klinger, A. Tonoyan, C. Leroy, and D. Sarkisyan, 'Hyperfine Paschen–Back regime of potassium D_2 line observed by Doppler-free spectroscopy,' Journal of Physics B: Atomic, Molecular and Optical Physics **51**, 145001 (2018).

[16] D. J. Whiting, E. Bimbard, J. Keaveney, M. A. Zentile, C. S. Adams, and I. G. Hughes, 'Electromagnetically induced absorption in a nondegenerate three-level ladder system,' Optics Letters **40**, 4289–4292 (2015).

[17] D. J. Whiting, J. Keaveney, C. S. Adams, and I. G. Hughes, 'Direct measurement of excited-state dipole matrix elements using electromagnetically induced transparency in the hyperfine Paschen-Back regime,' Physical Review A **93**, 043854 (2016).

[18] D. Whiting, N. Šibalić, J. Keaveney, C. Adams, and I. Hughes, 'Single-photon interference due to motion in an atomic collective excitation,' Physical Review Letters **118**, 253601 (2017).

[19] D. J. Whiting, R. S. Mathew, J. Keaveney, C. S. Adams, and I. G. Hughes, 'Four-wave mixing in a non-degenerate four-level diamond configuration in the hyperfine Paschen–Back regime,' Journal of Modern Optics **65**, 713–722 (2018).

[20] R. S. Mathew, F. Ponciano-Ojeda, J. Keaveney, D. J. Whiting, and I. G. Hughes, 'Simultaneous two-photon resonant optical laser locking (strolling) in the hyperfine Paschen–Back regime,' Optics Letters **43**, 4204–4207 (2018).

[21] A. L. Marchant, S. Händel, T. P. Wiles, S. A. Hopkins, C. S. Adams, and S. L. Cornish, 'Off-resonance laser frequency stabilization using the Faraday effect,' Optics Letters **36**, 64–66 (2011).

[22] D. J. Reed, N. Šibalić, D. J. Whiting, J. M. Kondo, C. S. Adams, and K. J. Weatherill, 'Low-drift Zeeman shifted atomic frequency reference,' OSA Continuum **1**, 4–12 (2018).

[23] F. Zi, X. Wu, W. Zhong, R. H. Parker, C. Yu, S. Budker, X. Lu, and H. Müller, 'Laser frequency stabilization by combining modulation transfer and frequency modulation spectroscopy,' Applied Optics **56**, 2649–2652 (2017).

[24] J.-B. Long, S.-J. Yang, S. Chen, and J.-W. Pan, 'Magnetic-enhanced modulation transfer spectroscopy and laser locking for [87]Rb repump transition,'

Optics Express **26**, 27773–27786 (2018).

[25] C. So, N. L. R. Spong, C. Möhl, Y. Jiao, T. Ilieva, and C. S. Adams, 'Zeeman-tunable modulation transfer spectroscopy,' Opt. Lett. **44**, 5374–5377 (2019).

[26] C. Möhl, N. L. R. Spong, Y. Jiao, C. So, T. Ilieva, M. Weidemüller, and C. S. Adams, 'Photon correlation transients in a weakly blockaded Rydberg ensemble,' arXiv:1910.13155 [physics] (2019). To appear in J. Phys. B: At. Mol. Opt. Phys. (2020).

[27] R. K. Raj, D. Bloch, J. J. Snyder, G. Camy, and M. Ducloy, 'High-frequency optically heterodyned saturation spectroscopy via resonant degenerate four-wave mixing,' Physical Review Letters **44**, 1251–1254 (1980).

[28] M. Ducloy and D. Bloch, 'Theory of degenerate four-wave mixing in reso-nant doppler-broadened media. - ii. Doppler-free heterodyne spectroscopy via collinear four-wave mixing in two- and three-level systems,' Journal de Physique **43**, 57–65 (1982).

[29] T. Preuschoff, M. Schlosser, and G. Birkl, 'Optimization strategies for modu-lation transfer spectroscopy applied to laser stabilization,' Optics Express **26**, 24010–24019 (2018).

[30] L. Zhe Li, S. Eon Park, H.-R. Noh, J.-D. Park, and C.-H. Cho, 'Modulation Transfer Spectroscopy for a Two-Level Atomic System with a Non-Cycling Transition,' Journal of the Physical Society of Japan **80**, 074301 (2011).

[31] H.-R. Noh, S. E. Park, L. Z. Li, J.-D. Park, and C.-H. Cho, 'Modulation transfer spectroscopy for ^{87}Rb atoms: theory and experiment,' Optics Express **19**, 23444–23452 (2011).

[32] B. H. Bransden, C. J. Joachain, and T. J. Plivier, *Physics of Atoms and Molecules* (Prentice Hall, 2003).

[33] D. A. Steck, 'Rubidium 87 D line data,' available online at http://steck.us/alkalidata (revision 2.2.1, 21 November 2019) .

[34] L. Weller, K. S. Kleinbach, M. A. Zentile, S. Knappe, C. S. Adams, and I. G. Hughes, 'Absolute absorption and dispersion of a rubidium vapour in the hyperfine Paschen–Back regime,' Journal of Physics B: Atomic, Molecular and Optical Physics **45**, 215005 (2012).

[35] M. A. Zentile, J. Keaveney, L. Weller, D. J. Whiting, C. S. Adams, and I. G. Hughes, 'ElecSus: A program to calculate the electric susceptibility of an atomic ensemble,' Computer Physics Communications **189**, 162–174 (2015).

[36] E. A. Whittaker, M. Gehrtz, and G. C. Bjorklund, 'Residual amplitude modulation in laser electro-optic phase modulation,' JOSA B **2**, 1320–1326 (1985).

[37] D. L. Carr, N. L. R. Spong, I. G. Hughes, and C. S. Adams, 'Measuring the Faraday effect in olive oil using permanent magnets and Malus' law,' European Journal of Physics (2019).

[38] D. Whiting, 'Nonlinear Optics in a Thermal Rb Vapour at High Magnetic

Fields,' Doctoral, Durham University (2017).

[39] M. Zentile, 'Applications of the Faraday Effect in Hot Atomic Vapours,' Doctoral, Durham University (2015).

[40] L. Weller, 'Absolute Absorption and Dispersion in a Thermal Rb Vapour at High Densities and High Magnetic Fields.' Doctoral, Durham University (2013).

[41] S. Zienau, 'Optical resonance and two level atoms,' Physics Bulletin **26**, 545–546 (1975).

[42] P. W. Milonni and J. H. Eberly, *Lasers* (Wiley, New York, 1988). OCLC: 16801324.

[43] C. J. Bordé, J. L. Hall, C. V. Kunasz, and D. G. Hummer, 'Saturated absorption line shape: calculation of the transit-time broadening by a perturbation approach,' Physical Review A **14**, 236–263 (1976).

[44] J. E. Thomas, M. J. Kelly, J. P. Monchalin, N. A. Kurnit, and A. Javan, 'Transit-time effects in power-broadened Doppler-free saturation resonances,' Physical Review A **15**, 2356–2365 (1977).

[45] S. G. Rautian and A. M. Shalagin, 'Saturation effects for long-lived systems in spatially bounded fields,' Journal of Experimental and Theoretical Physics **31**, 518 (1970).

[46] E. V. Baklanov, B. Y. Dubetskii, V. M. Semibalamut, and E. A. Titov, 'Transit width of a nonlinear power resonance in low-pressure gases,' Soviet Journal of Quantum Electronics **5**, 1374 (1975).

[47] N. V. Vitanov, B. W. Shore, L. Yatsenko, K. Böhmer, T. Halfmann, T. Rickes, and K. Bergmann, 'Power broadening revisited: theory and experiment,' Optics Communications **199**, 117–126 (2001).

[48] W. Demtröder, *Laser Spectroscopy: Vol. 1: Basic Principles* (Springer Science & Business Media, 2008).

[49] W. Riley and D. A. Howe, 'Handbook of Frequency Stability Analysis | NIST,' Special Publication (NIST SP) - 1065 (2008).

[50] D. W. Allan, 'Statistics of atomic frequency standards,' Proceedings of the IEEE **54**, 221–230 (1966).

[51] A. D. Ludlow, M. M. Boyd, J. Ye, E. Peik, and P. Schmidt, 'Optical atomic clocks,' Reviews of Modern Physics **87**, 637–701 (2015).

[52] O. Schmidt, K. M. Knaak, R. Wynands, and D. Meschede, 'Cesium saturation spectroscopy revisited: How to reverse peaks and observe narrow resonances,' Applied Physics B **59**, 167–178 (1994).

[53] A. D. Cronin, J. Schmiedmayer, and D. E. Pritchard, 'Optics and interferometry with atoms and molecules,' Reviews of Modern Physics **81**, 1051–1129 (2009).

[54] D. A. Steck, 'Rubidium 85 D line data,' available online at

http://steck.us/alkalidata (revision 2.2.1, 21 November 2019) .

A ^{85}Rb atomic structure

Naturally occurring rubidium consists of two isotopes: rubidium 85, the only stable isotope of rubidium; and radioactive rubidium 87, which decays extremely slowly and is therefore effectively stable. Like ^{87}Rb, ^{85}Rb has 37 electrons, only one of which is in the outermost shell. Since many of an atom's physical and optical properties are determined by the valence electron, much of what was discussed in Section 2.2.1 remains relevant here.

The level structure diagram of the ^{85}Rb D$_2$ transition is presented in Fig. A.1. The gross structure is determined by the principal quantum number n and the orbital angular momentum of the electron L. Due to the spin–orbit interaction [Eqn. 2.2.5], these terms are further split into fine-structure levels labelled by the total angular momentum quantum number $J = 1/2$ for the ground state, and $J = 1/2$ or $3/2$ for the first excited state. The resultant transition, $5^2\mathrm{S}_{1/2} \to 5^2\mathrm{P}_{3/2}$, will be the only transition we consider hereafter.

On top of the fine structure splitting, the further coupling between the total electronic angular momentum **J** and nuclear spin angular momentum **I** gives rise to a much smaller effect termed the 'hyperfine' structure [Eqn. 2.2.7]. For the ground state in ^{85}Rb, $J = 1/2$ and $I = 5/2$, so $|J - I| \leq F \leq J + I$ can take values 2 or 3. In the absence of any external fields, there are $2F + 1$ degenerate magnetic sublevels m_F for each F state:

$$F = 2,\ m_F = -2, -1, 0, +1, +2$$
$$F = 3,\ m_F = -3, -2, -1, 0, +1, +2, +3.$$

For the $5^2\mathrm{P}_{3/2}$ excited state, the possible values of F' range from $|3/2 - 5/2| = 1$ to $|3/2 + 5/2| = 4$. The degeneracy of each of the individual F' state occurs as below:

$$F' = 1,\ m_{F'} = -1, 0, +1$$
$$F' = 2,\ m_{F'} = -2, -1, 0, +1, +2$$
$$F' = 3,\ m_{F'} = -3, -2, -1, 0, +1, +2, +3$$
$$F' = 4,\ m_{F'} = -4, -3, -2, -1, 0, +1, +2, +3, +4.$$

The degeneracy of $2F + 1$ per F state breaks down as the magnetic field B (and by extension $\hat{\mathcal{H}}_B$) becomes non-zero: this is just the Zeeman effect. The magnetic field dependence of the ground and excited states of the ^{85}Rb D$_2$ transition are shown respectively in Figs. A.2 and A.3. The Zeeman shifts of the transition frequencies
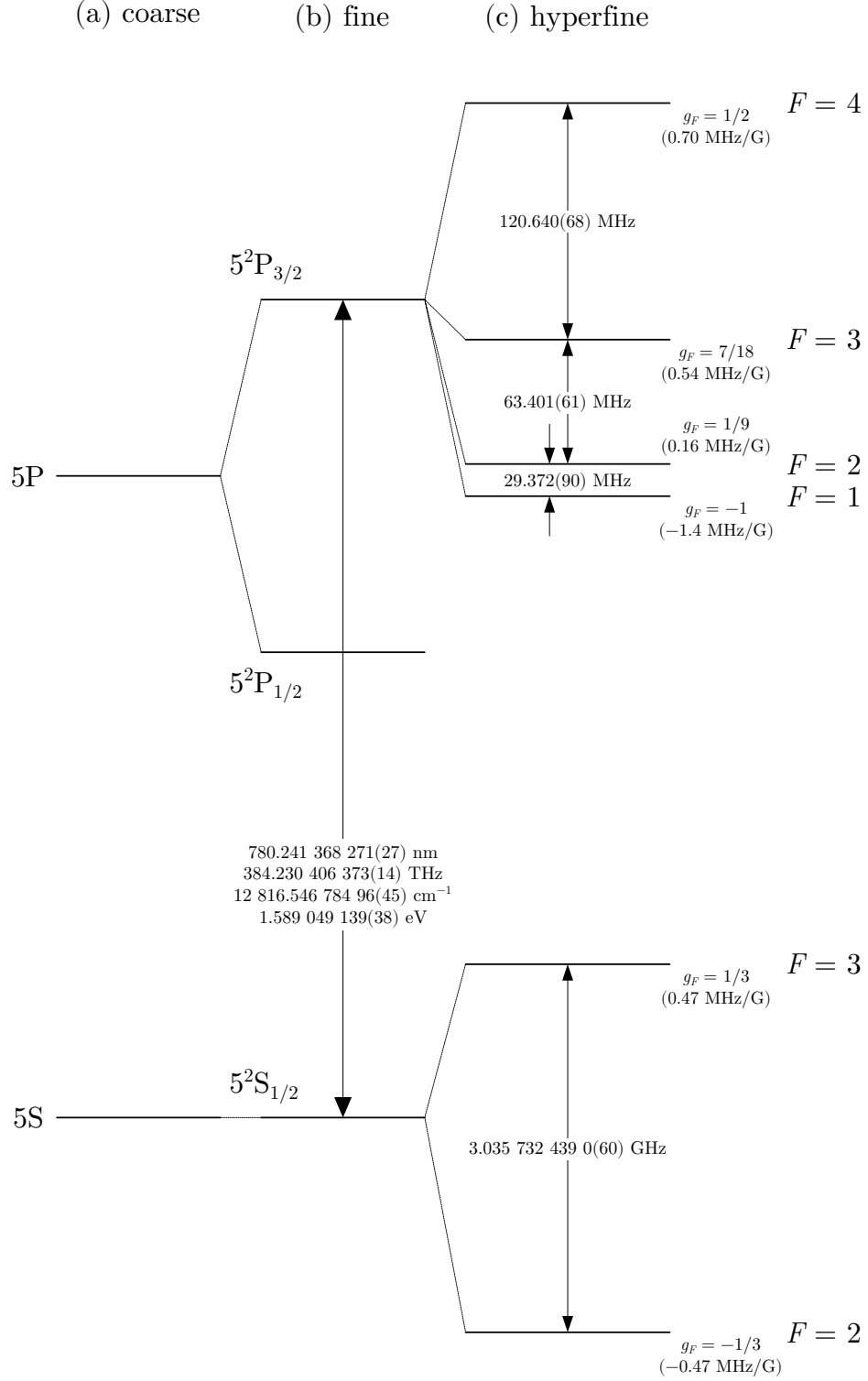
are depicted in Fig. A.5.

(a) coarse   (b) fine   (c) hyperfine

**Figure A.1 | Unperturbed (a) coarse, (b) fine, and (c) hyperfine struc-
ture diagram of the ^{85}Rb D$_2$ transition.** The approximate
Landé g_F-factors for each individual F state are provided, along
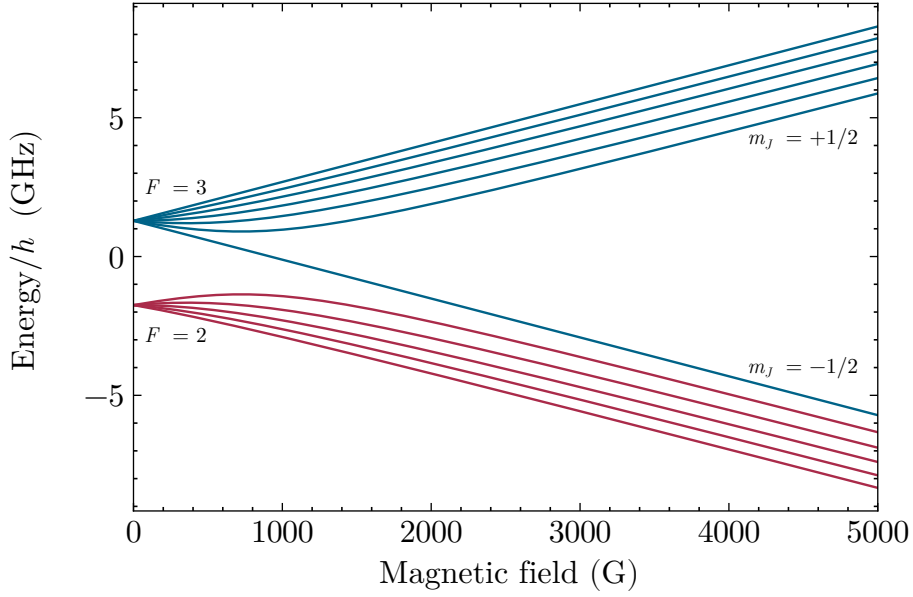with the Zeeman splittings between adjacent m_F levels. Adapted
from [54].

Figure A.2 | Magnetic field dependence of the $5^2S_{1/2}$ ground state of ^{85}Rb. The quantum number F loses its validity with increasing magnetic field until m_J, m_I become good descriptors of the eigenstates.
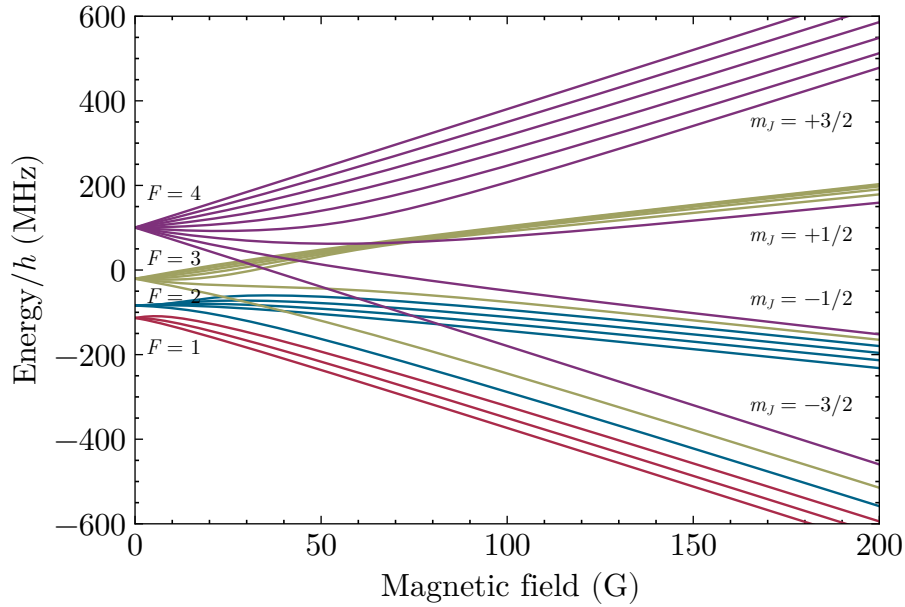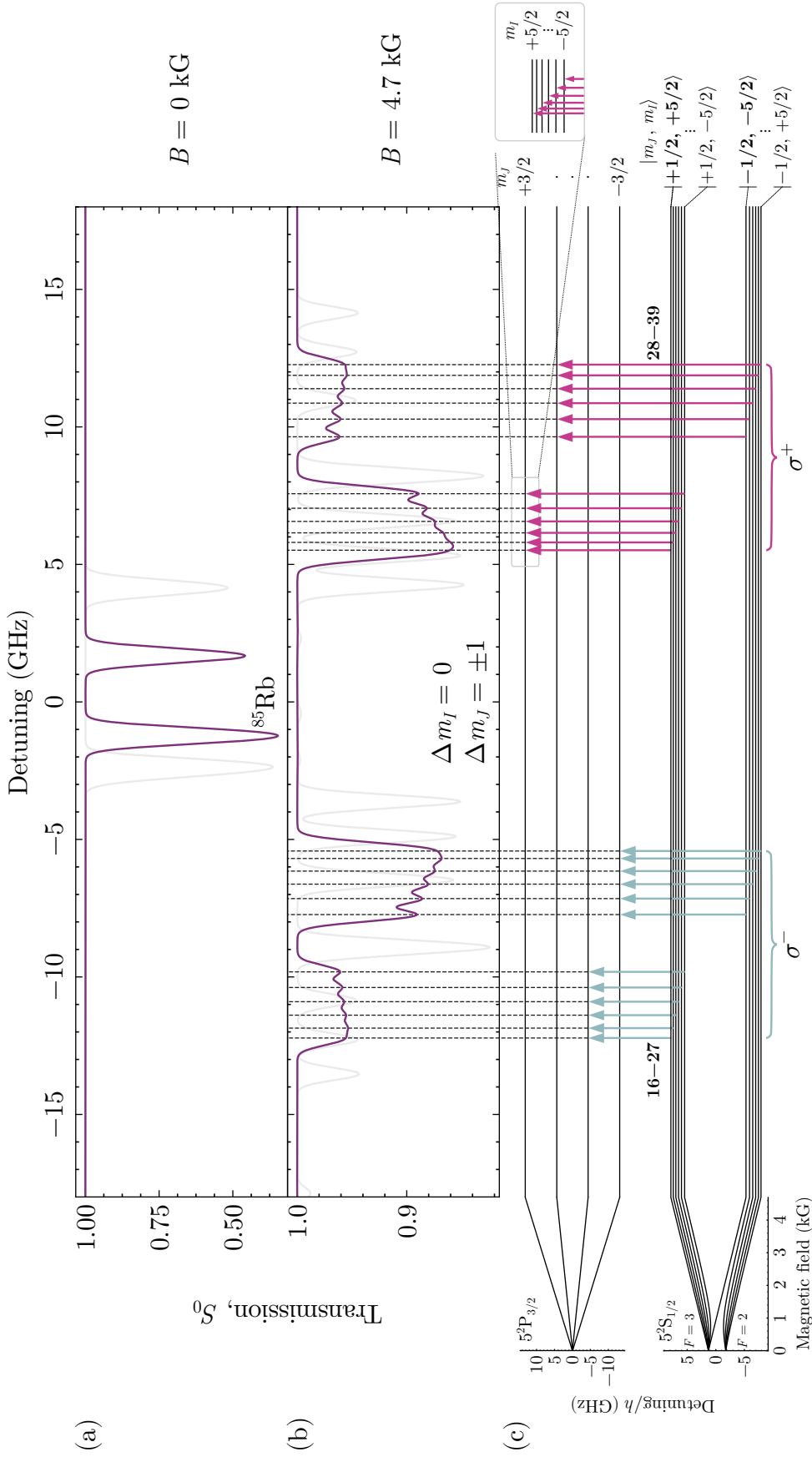

Figure A.3 | Magnetic field dependence of the $5^2P_{3/2}$ excited manifold of ^{85}Rb. The quantum number F loses its validity with increasing magnetic field until m_J, m_I become good descriptors of the eigenstates.

Figure A.4 | Theoretical weak-probe spectra for the ^{85}Rb D$_2$ line at (a) $B = 0$ and (b) 4.7 kG with linear polarisation. In zero external B-field, (a), the two absorption lines correspond to the two hyperfine ground states $F = 2, 3$. The hyperfine transitions ($F \rightarrow F'$, $F \rightarrow F' - 1$, $F \rightarrow F' + 1$) are unresolved within each Doppler-broadened band. In (b) we are in the HPB regime, where nearly all transitions are resolvable and correspond to those indicated by the vertical arrows in the energy level diagram (c). The eigenstates of the system are labelled in the $|m_J, m_I\rangle$ basis with the basis state that dominates its composition at high magnetic fields, with the stretched states marked in bold. For reference, the ^{87}Rb spectra are shown in the background in grey. Created with ElecSus in Python [35].
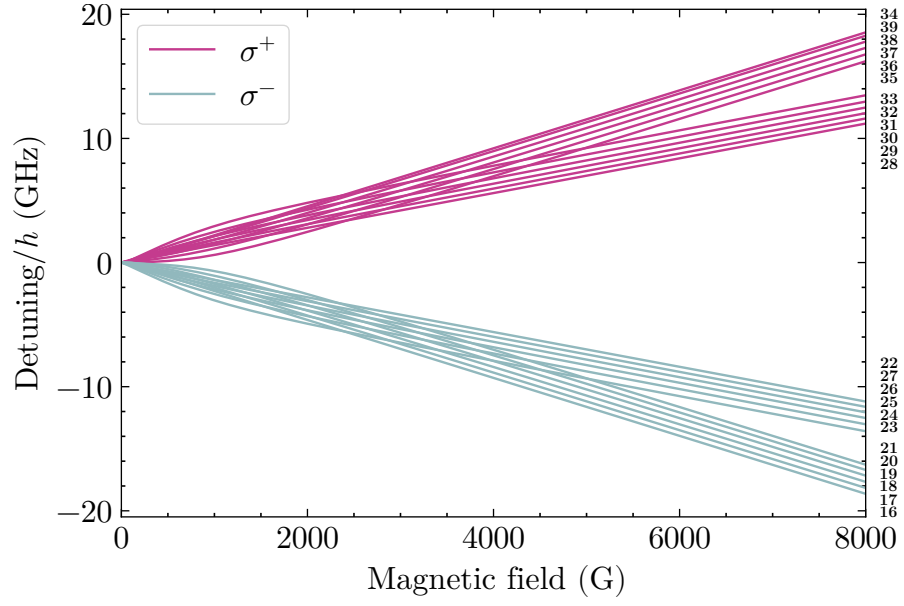
Figure A.5 | Zeeman shift of the ^{87}Rb D$_2$ transition for the absorption of σ^+ (pink) and σ^- (blue) light. Here, detuning refers to frequency shifts of individual transitions as a result of the applied field. Numbers denote the corresponding transitions depicted in Fig. A.4.

B   B-roll

B-roll are figures I would like to have seen make into the thesis, but which for various reasons did not.
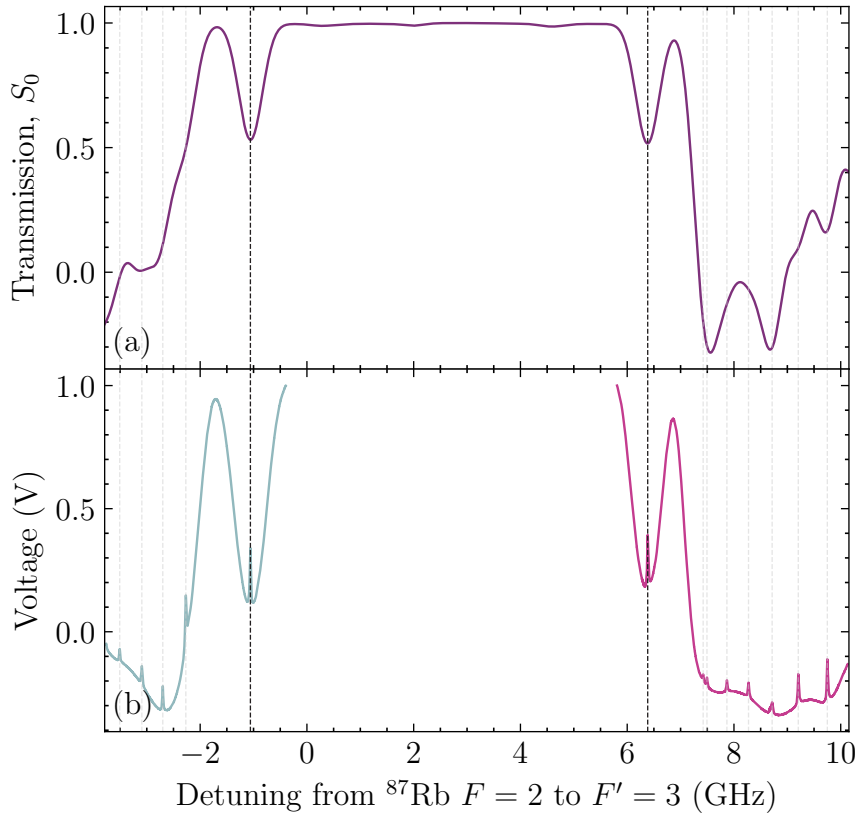
Chapter 4

Figure B.1 | (a) ElecSus-predicted weak-probe versus (b) experimental Doppler-free spectra at $B = 4.5\,\mathrm{kG}$. The dotted lines show the location of the spectral features from the experimental traces, with the 'main' features in Figs. 4.1 and 4.3 indicated in black. While intuitively one would expect the greatest error signal to occur where the optical depth is greatest, the medium is so optically thick in regions (for instance, where transitions due to ^{87}Rb and ^{85}Rb coincide) that the closed transitions become buried.
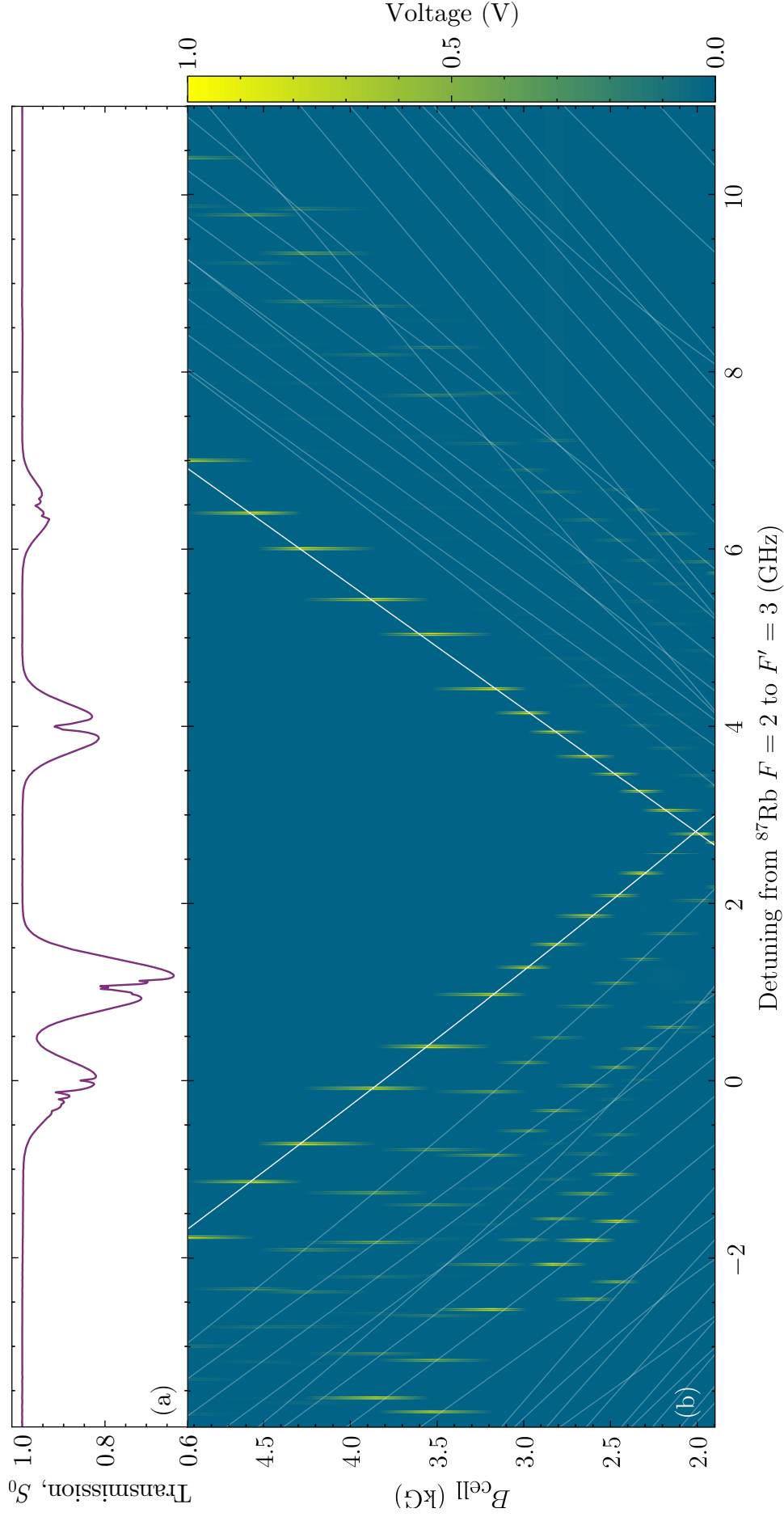
Figure B.2 | Contour plot of the ZMTS error signals as a function of magnetic field strength, (b). The size of the ZMTS features (maximal feature normalised to 1.0 V) are shown in the plot as varying shades of yellow.
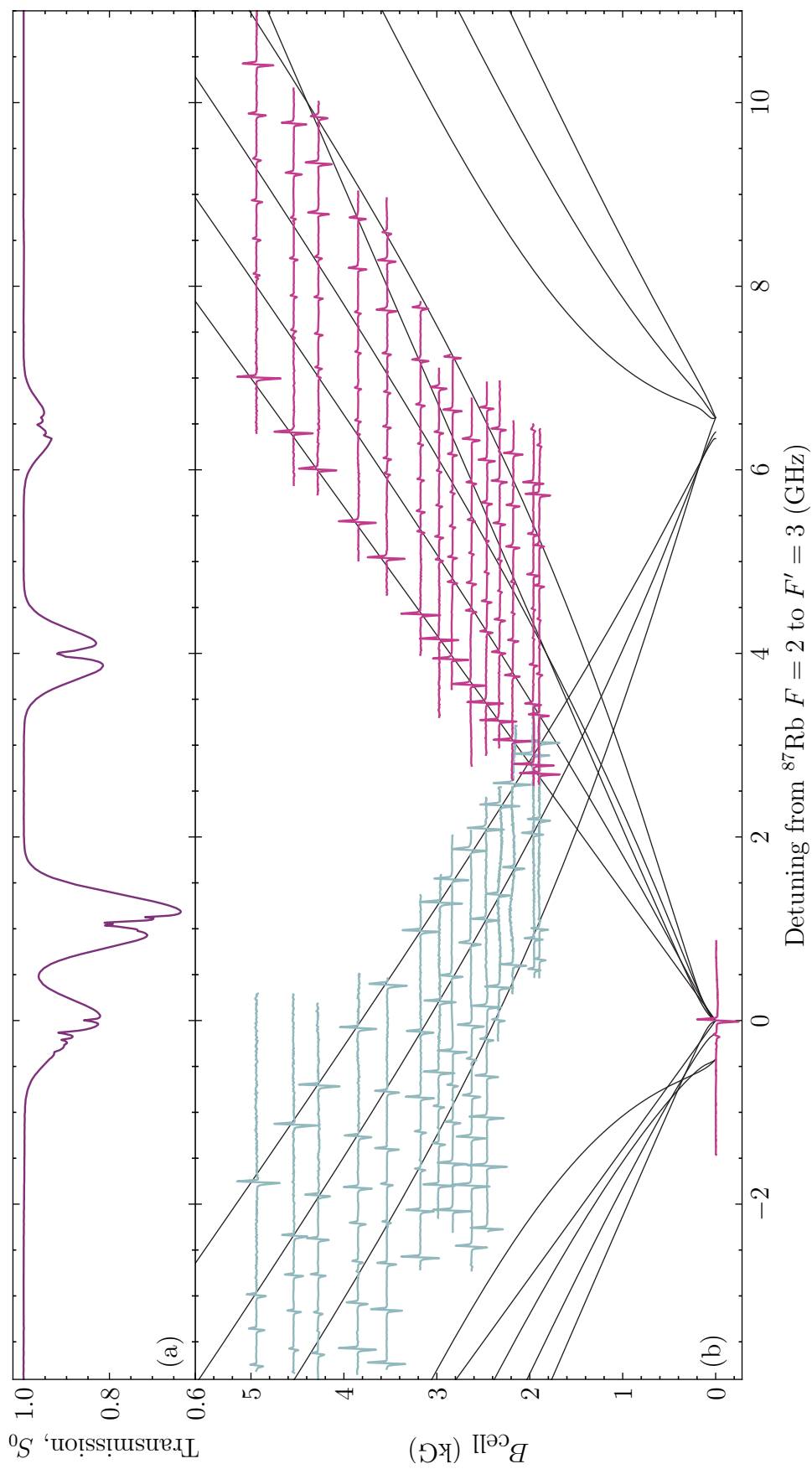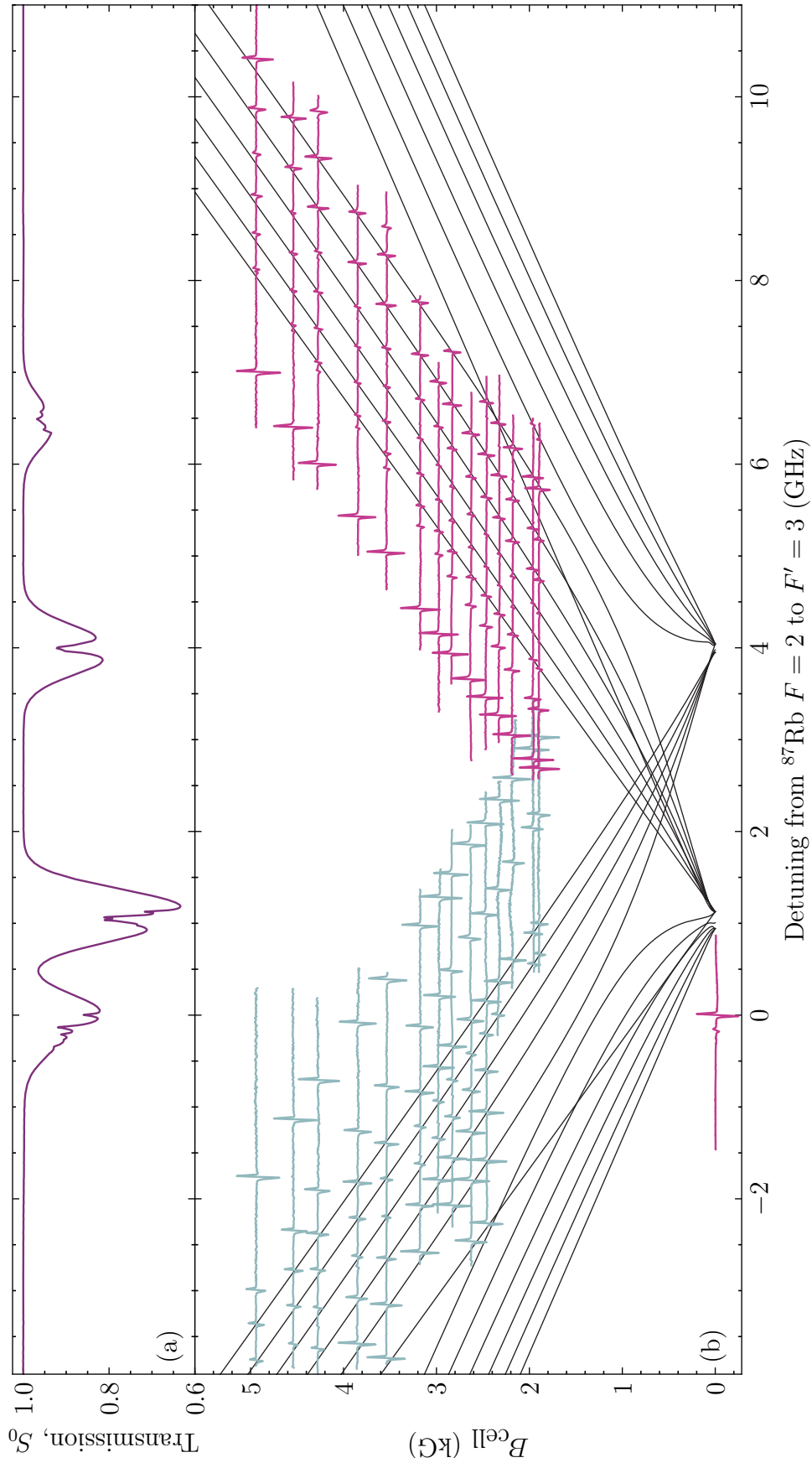
Figure B.3 | Fig. 4.3, with rubidium 87 lines only.

Figure B.4 | Fig. 4.3, with rubidium 85 lines only.